ABSTRACT

RISENMAY, MATTHEW ALLAN: Application of Supervised Machine Learning to Search for Nuclear Fallout Analytes that Identify Explosive Type. (Under the direction of Dr. John Mattingly).

In the event of a nuclear explosive attack from and unknown source, rapid and accurate characterization of the explosion to facilitate attribution is critical. A known reliable characterization capability can also improve deterrence. Current forensic analysis mainly uses lab-based mass spectroscopic methods that can require many days to weeks for collection, preparation, and analysis. During this time, key evidence in the form of short-lived fission products decays away and precious data are lost. On-site gamma spectroscopy provides prompt data during collection, but the data are sufficiently complex that routine analysis cannot accurately characterize the fissile isotope and neutron spectrum of the explosion.

This thesis evaluates an approach for rapidly characterizing the main fissile isotope (U-235 or Pu-239) and neutron spectrum (lower energy fission or higher energy fusion) of a nuclear explosive through the application of supervised machine learning to predictions of post-detonation nuclear debris (a.k.a. fallout) composition. The data used were fission product activity per gram of fallout from simulated nuclear explosions. The machine learning methods employed were decision tree, random forest, and gradient boosting.

Previous research showed that variance in fallout composition can be reduced by controlling the particle size of the collected fallout. Additionally, a surrogate model of the Defense Land Fallout Interpretive Code (DELFIC) accurately reproduced results from the code while greatly reducing the computational burden of fallout simulation. This development also enabled uncertainty propagation of thermodynamic parameters through direct sampling.

Large data sets of nuclear fallout isotopes and their activities were produced with these tools. These data were analyzed using machine learning methods to find combinations of nuclides to robustly characterize the main fissile isotope and neutron spectrum.

© Copyright 2023 by Matthew Allan Risenmay

All Rights Reserved

Application of Supervised Machine Learning to Search for Nuclear Fallout Analytes that Identify Explosive Type

by
Matthew Allan Risenmay

A thesis submitted to the Graduate Faculty of
North Carolina State University
in partial fulfillment of the
requirements for the degree of
Master of Science

Nuclear Engineering

Raleigh, North Carolina
2023

APPROVED BY:

_____	_____
Dr. John Mattingly Committee Chair	Dr. Mohammed Bourham
_____	
Dr. Alexander Bataller	

DEDICATION

This work, and indeed all the work I do, is dedicated to my family.

BIOGRAPHY

Matthew Risenmay was raised in Maysville, Kentucky. He earned his Bachelor and Master of Science in Mechanical Engineering from Brigham Young University – Idaho in 2004 and New Mexico School of Mines and Technology in 2008 respectively. He worked as an Explosives Engineer at Sandia National Labs from 2004-2010. Matthew commissioned as an Active-Duty Infantry Officer in the United States Army in 2011. He completed combat tours and leadership roles in the 4th Infantry Division and 75th Ranger Regiment, and three Commands in the 82nd Airborne Division. He was selected in 2020 to become a Functional Area 52 (Nuclear Counter-Proliferation) Officer.

Matthew is currently in the Master of Science program for Nuclear Engineering at North Carolina State University. He enjoys his roles as a husband and a father of four children, and with his family he enjoys reading, working, exercising, service, and traveling. His wife, Angela Packer Risenmay, has her bachelor's degree in secondary math education and serves the community as a volunteer leader of a large local women's organization. They were married in 2002.

ACKNOWLEDGMENTS

This work could not have been possible without the guidance, patience, and dedicated instruction of my academic advisor, Dr. John Mattingly. I am grateful to him for the thoughtfulness, commitment, encouragement, and direction he has provided throughout the past two years. Many members of the RADIANS research team past and present also provided timely and valuable assistance through this process. My mentors and leaders in the U.S. Army were pivotal in providing me the opportunity to pursue this education and research, helping to instill the confidence and drive needed pursue this goal. Support, inspiration, and encouragement from my singular and remarkable wife and understanding children are foundational to all the work I accomplish, of which this is only a small part.

TABLE OF CONTENTS

LIST OF TABLES

LIST OF FIGURES

CHAPTER 1: INTRODUCTION

1.1 Motivation

Rapid technical forensic analysis of post-detonation nuclear debris, a.k.a. fallout, is important to identifying the explosive's provenance. This research focuses on rapid post-detonation forensic analysis of a nuclear device. Specifically, it investigates the application of supervised machine learning to predictions of fallout composition based on the Defense Land Fallout Interpretive Code (DELFIC) maintained by Oak Ridge National Laboratory. [1]

The field of nuclear forensics originated in the 1990s when nuclear and other smuggled radioactive materials were interdicted in the former Soviet Union and Eastern Europe following the end of the Cold War. [2] Following the September 11, 2001 attacks by al Qaeda, federal organizations placed heightened priority on developing rapid post-detonation forensic analyses. Two key characteristics of a nuclear explosive include (1) the type of fissile material fueling the runaway fission chain reaction, and (2) the spectrum of neutrons inducing fission. These characteristics can (1) differentiate between uranium and plutonium-based explosives, and (2) differentiate between a basic fission explosive and a more sophisticated explosive employing fusion boosting. These characteristics can help narrow the field of likely perpetrators when correlated with technical intelligence of adversary capabilities. The radiological evidence left behind is actively decaying post-detonation; consequently, time is of the essence.

The ability to accelerate characterization of the fissile material and neutron spectrum of a nuclear explosive post-detonation is valuable to a government or an alliance that is under political pressure to attribute the attack, respond to it, and protect its constituents from further

harm. A demonstrated ability to rapidly characterize and attribute a nuclear explosive's provenance serves to deter would-be aggressors.

Recent world events reinforce the need for progress in the field of nuclear forensics. Since 2022, Iran has deactivated safeguards cameras at nuclear sites while they continue to illicitly expand deeply buried tunnel networks near the Natanz nuclear site. [3] [4] Regarding North Korea, the U.S. ambassador to the United Nations stated that the country, "has engaged in an unprovoked series of 23 ballistic missile launches since the start of 2022 and is actively preparing to conduct a nuclear test." [5] Russia invaded the sovereign nation of Ukraine in late February 2022 and have waged war on them for many months now in the face of heavy and united NATO condemnation. [6] China continues to expand its nuclear arsenal and military at an unprecedented rate. [7] Many of the earlier concerns that energized advancements in nuclear forensic science have returned and metastasized.

Vayl Oxford, who recently directed the Defense Thread Reduction Agency stated, "Nuclear forensics is now increasingly recognized as having the potential to serve as a central pillar of deterrence in the 21st century. Nuclear forensics underpins the attribution process by helping to identify the possible sources of materials or devices, the device design, or the pathway taken to the actual incident. Attribution will be derived from the fusion of the technical nuclear forensics analysis, with all-source intelligence, and law enforcement information to enable the decision-making process." [8]

1.2 Background

The field of post-detonation nuclear forensics has relied on lab-based sample preparation that include chemical separation and other processes for microscopic, radiographic, and mass spectrometric measurements. These techniques enable detailed analyses of the samples, but fallout is principally composed of glassy particles, and sample preparation for these measurements often takes a week or longer. [9] Cassata et al. stated, “The fundamental challenges facing post-detonation nuclear forensics are centered around the need for rapid and accurate analyses of debris samples,” and, “advanced data analytics such as machine learning to enhance early-time gamma-spectrometry analysis could significantly impact measurement and reporting timelines by speeding up accurate interpretation of complex gamma signals collected in the field or the laboratory.” [10]

Speeding the process of post-detonation analytics is challenging because there are no recent post-detonation samples to test the techniques against following the Comprehensive Nuclear Test Ban Treaty of 1996. Consequently, the composition of nuclear debris must be simulated, either by numerical calculations or surrogate experiments, that approximate the actual conditions in a nuclear explosion. These constraints make the development of robust tools that factor uncertainty in the analysis essential to advancing these incipient forensic methods.

The goal of this thesis is to advance ongoing work in the rapid characterization of a nuclear explosive post-detonation by applying supervised machine learning techniques to simulations of fallout formation incorporating large parameter uncertainties. Specifically, decision tree, random forest, and gradient boosting machine learning methods were applied to classify fallout composition by fissile material and neutron spectrum. U-235 and Pu-239 were the two fissile materials considered. The neutron energies considered were fission-spectrum neutrons

(ranging from thermal to several MeV) and fusion-spectrum neutrons (high-energy 14.1 MeV from D + T fusion). Application of these tools to gamma spectrometry could provide classification results within minutes or hours of obtaining the nuclear debris sample. The effectiveness of the classification models is discussed.

1.3 Prior Work

Early efforts in the 1950's and 1960's to understand fallout formation and fractionation involved collecting fallout from atmospheric testing of nuclear weapons near ground level [11] The Partial Nuclear Test Ban Treaty was signed in 1963 effectively ending experimental analysis of nuclear fallout.

Empirical modeling from the limited test data identified relationships between fallout composition and particle size. Heft concluded that the distributions of volatile and refractory products could be determined by analyzing samples separated by size, and that the behavior of all fission product nuclides can be related to a single pair of nuclides, one being volatile and the other refractory. [12]

In a departure from the empirical modeling that preceded it, Korts and Norman proposed a computational method to incorporate thermodynamic chemical principles into modeling fractionation behavior in 1967. They employed Henry's law and diffusion theory to model condensation and diffusion of fission products into cloud debris [13]

Improvements in computational power and methods combined with the complete cessation of nuclear testing following the Comprehensive Nuclear Test-Ban Treaty in 1996 increased emphasis on computational modeling of fallout formation. The Oak Ridge Isotope Generation (ORIGEN-S) code was used by Smith to model gamma emissions from the fission of

U-235, U-238, and Pu-239. [14] Smith then modeled detector response to these gamma emissions using the Gamma Detector Response and Analysis Software (GADRAS) developed and maintained by Sandia National Laboratories. [15] She demonstrated that using ratios of gamma photopeaks from different fission products enabled prompt characterization of nuclear fallout. [16] These calculations, however, did not account for uncertainties in the properties of the fission products.

Miller built on Smith's work by coupling ORIGEN-S calculations with the Los Alamos National Laboratory Monte Carlo N-Particle Transport Code (MCNP5) to simulate the gamma spectra. [17] [18] Miller incorporated counting uncertainties and compared his calculations to reactor-irradiated fissile materials from Pacific Northwest National Laboratory. Miller found that gamma photopeaks could also be used to characterize fissile material and neutron spectrum, but he compared only refractory samples with the unfractionated reactor samples. This provided further proof of concept for prompt characterization of nuclear fallout but did not adequately capture the effects and uncertainties associated with fractionation.

Lucero used the Department of Defense Land Fallout Interpretive Code (DELFIC) to predict fallout composition from hundreds of simulated nuclear detonations with varied device characteristics, atmospheric conditions, and sampling conditions. [19] [1] Lucero varied explosive yield, burst height, wind speed, sample collection location, sample collection time, and particle size. He demonstrated that most of the variance in the fallout gamma spectrum resulting from fractionation can be eliminated by controlling fallout particle size. In other words, by controlling fallout particle diameter, variance in composition due to fractionation of volatile and refractory species can be significantly reduced.

Gifford extended the previous work by employing a physical model of fallout formation instead of an empirical model. [20] The physical model enabled uncertainties in fallout composition to be quantified. Gifford used the Korts and Norman (KN) thermodynamic model of fallout formation implemented in DELFIC, and he propagated uncertainties in the model parameters onto the predicted fallout composition. Due to the computational expense of the KN model, which has several hundred input parameters, Gifford developed surrogate models using global sensitivity analysis, active subspace decomposition, and regression modeling. His analysis identified which Henry's Law and diffusion equation coefficients influenced the uncertainty in the predicted composition. The surrogate models were used to propagate increasing levels of uniformly distributed random samples of the thermodynamic parameters up to ±50% of their nominal values.

Gifford's surrogate models produced predictions with less than 3% mean absolute percentage error from the physical model, and they reduced computational time by five orders of magnitude. This enabled direct sampling uncertainty propagation for large numbers of simulated nuclear explosions. Gifford identified 12 radionuclides as the best candidates for classifying fissile material and neutron spectrum. His work, however, was limited to analyzing single nuclides.

In a recent study by Lawrence Livermore National Laboratory (LLNL), Dardenne et al. examined an expanded historical dataset and compared it with Freiling number fractionation models in use for decades. They concluded that the assumptions guiding these models of fractionation are insufficient to provide reliable predictions, and that data from nuclear events show little reliable correlation from event to event in terms of chemical fractionation. [21] They found no consistent dependence of fractionation on the energy output of nuclear explosions; this

being the basis for temperature/time profiles that dictated condensation in Frieling models. They theorized that highly influential secondary factors are not captured by generalizations used in much of today's modeling for chemical fractionation; that the complexity of fractionation from event to event could include other highly influential factors like differences in surrounding materials and fireball confinement by structural or environmental factors. They stated that fractionation consistency from event to event, within a mass chain, or for a single nuclide cannot be assumed. Dardenne et al. acknowledged that previous approaches were cutting edge for their age, and they advocated for a deeper look into past data with new methods to improve understanding and predictions of chemical fractionation for varied events. They advocate for implementation of uncertainties and methods like principal component analysis to discover more robust linkages in testing data to improve future models.

Problematically, Dardenne et al. did not evaluate prediction methods like the KN model that can account for additional factors they identified as possibly important, but rather was based on Freiling empirical models and evaluated against extrapolated trendlines from sparse experimental data. The KN model can incorporate a greater variety of materials in the debris cloud and simulate confinement by modeling parts of the cloud separately.

The gap between the physics of fallout formation and available models is widely acknowledged, as is their utility given judicious application. The British statistician George Box is attributed with the aphorism, "All models are wrong, but some are useful". The LLNL critique focused on confirming what is wrong in Freiling number fractionation models. This research employed machine learning to KN model fallout prediction tools, classifying explosive type despite large uncertainties in thermodynamic parameters and assuming no knowledge of explosive yield or burst height.

1.4 Novel Contributions

This thesis explores methods for prompt characterization of nuclear explosions by application of supervised machine learning. Specifically, it applied the surrogate model developed by Gifford that enabled uncertainty propagation to produce a large number of randomized predictions of fallout composition. Supervised machine learning classification algorithms were trained to identify patterns in groups of radionuclides that can distinguish explosive fissile material and neutron spectrum.

A large uncertainty level of ±50% in thermodynamic properties was maintained throughout to demonstrate robustness of the method, and the work maintained its focus on 12 radionuclides that demonstrate large separation between different explosive classes. The most valuable outputs of this work are (1) an evaluation of the effectiveness of employing machine learning methods to classify explosive type and (2) practical recommendations for identifying and linking observable gammas in fallout gamma spectra with classification tools.

1.5 Organization

Chapter 2 discusses the processes that affect fallout composition, which formed the basis of this research. In Chapter 3, the methods employed for synthesizing and analyzing predictions of fallout composition are presented. Chapter 4 presents and discusses the results of the analysis. Chapter 5 summarizes the accomplishments of this work, draws a few conclusions, and makes recommendations for future work.

CHAPTER 2: FALLOUT FORMATION

2.1 Fissions and Fission Yield Curves

Post-detonation forensic analysis using gamma spectroscopy has primarily focused on the analysis of isotopic ratios. This is normally done by separating sampled radionuclides using radiochemistry in a laboratory, which can require a week or more. During that time, the radionuclides continue to decay and information is lost. Using gamma spectroscopy to conduct isotopic ratio analysis obviates the need to chemically separate the radionuclides, which would enable similar results to be obtained shortly after sample collection. The difficulty comes in the complexity of measuring the numerous radionuclides simultaneously present in an unseparated sample.

The quantity of gamma emission is directly related to the radioactivity and quantity of the radionuclide. The ratios of two or more radionuclides produced by a nuclear explosion can be used in comparison with known fission yield curves to characterize fissile material and neutron spectrum. As shown in Figure 1, there are clear separations in fission product yield (vertical axis) that occur as mass number (horizontal axis) changes. Note the higher yield of fission products between the mass numbers of 108 and 129 for higher-energy neutrons characteristic of a fusion spectrum. This occurs because nearly equal-mass fission fragments become more probable as neutron energy increases. Also observe the more massive Pu-239 nucleus yields a greater quantity of light fission products with higher mass.

The fission products produced by of U-235 and Pu-239 are neutron rich and undergo beta-decay. Beta decay increases the atomic number of a radionuclide while the mass number

remains constant. When this happened successively in a series, the beta decay series progress in a “mass chain” from the original fission product.

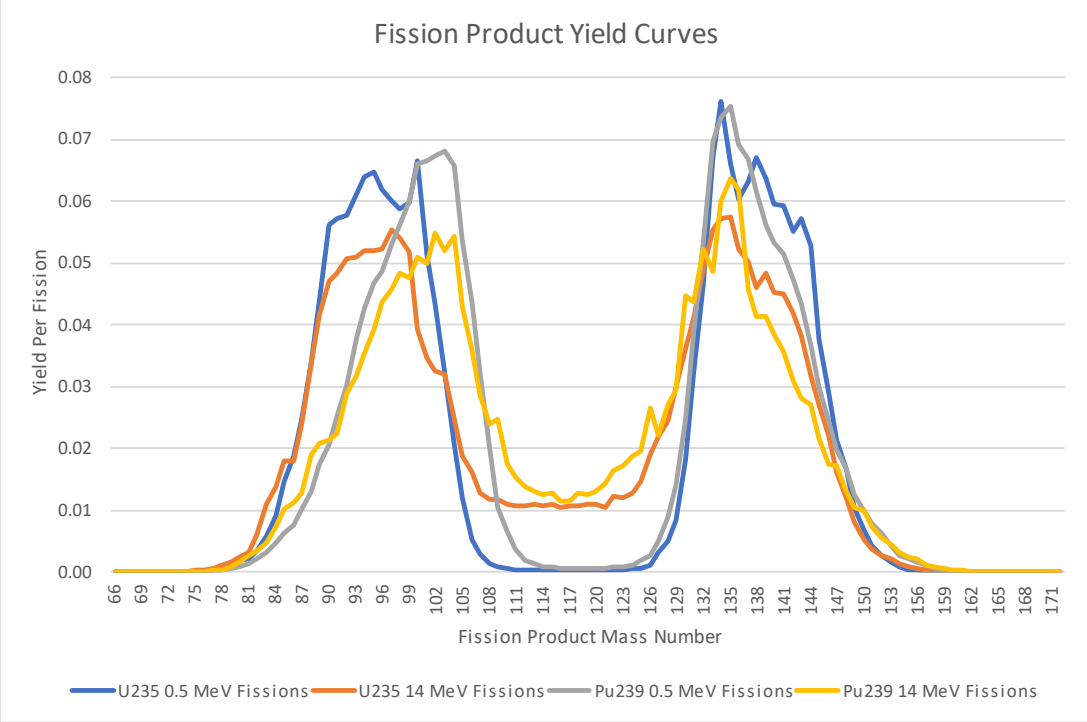

Figure 2.1 Fission yield curves by fissile isotope and neutron spectrum. Data for curves pulled from JAEA. **[22]**

In a single fission of U-235 induced by a 0.5 MeV neutron, an atom in the 95-mass chain is produced with about 6.5% likelihood. [22] Assuming the radioisotope Kr-95 is the initial light fission fragment, Kr-95 and its beta-decay progeny will undergo beta-minus decays along its atomic mass chain towards stability. Kr-95 will never realistically be captured in a fallout sample because its half-life is remarkably short (114 ms). In fact, Kr-95 and its progeny will likely undergo four beta-minus decays in the first half hour (the four radionuclides in this mass chain from Kr-95 to Y-95 have a combined half-life of less than 11 minutes) and become Zr-95 which has a half-life of about 64 days. [23] It is this atom of Zr-95 that is likely to be sampled from the

fallout debris in the near-term period following the explosion. Another heavier radioisotope of Barium will have been created from the same fission reaction (conserving all 92 protons of uranium), likely in a mass chain near 139 depending on how many fission neutrons were released in the specific fission reaction. Ba-139 has a half life of about 1.4 hours, so it will likely decay to stable La-139 before sampling occurs.

Beta-minus decay usually leaves the new nucleus in an excited state that will de-excite by releasing gamma rays, each with its own discrete energy and probability (or intensity). Detection of these characteristic gamma energies can be used to identify the radionuclides present in the sample. As discussed above, analyzing ratios of the intensity of these characteristic gammas can be used to estimate relative amounts of fission products in the sample. If the sample were representative of the fission product quantities produced by the explosion, then one could take the proportions in the sample and reference the fission product yield curve to identify the fissile material and neutron spectrum. However, radionuclide proportions in nuclear fallout are not representative of the proportions produced in the explosion. This disparity arises from fractionation.

2.2 Fractionation

Fractionation is a complicating process in fallout formation. Specifically, fractionation alters how fission products are concentrated in fallout samples, causing fallout composition to vary based on sample size and location. Freiling described the process of fractionation as, “any process which causes the radionuclide composition of a sample of nuclear debris to be unrepresentative of the debris taken as a whole”. [11] Thus, the proportions given in fission yield curves cannot be used as a practical model for classifying a real sample of nuclear debris.

When a nuclear explosion occurs close to the ground, large amounts of soil are lofted into the air with the vaporized fission products and other bomb materials. Some of this soil entrained in the fireball will be melted and some vaporized depending on proximity to the explosion and the temperature of the fireball. [24] As the fireball rises and cools, the radioactive fission products continue to decay into new radionuclides along their mass chains. Elements with higher condensation temperatures will begin to condense and diffuse through molten soil particles in the debris cloud. The soil solidification temperature (SST) is approximately 2200 degrees Kelvin for siliceous soils. [1] Refractory radionuclides that condense at temperatures higher than the SST form particles with soil that are larger and vitrified. These particles have a fairly uniform volumetric distribution of refractory fission products.

As the fireball continues to cool below the SST, soil particles solidify before the remaining fission products have reached their condensation temperature. These still-vaporized radionuclides are volatile, and eventually they reach their condensation temperature below SST, and mainly condense on the outer surface of solidified debris particles. Fractionation that depends on the condensation temperature of materials is called chemical fractionation.

There is an additional process that occurs due to gravity and weather patterns. This type of fractionation is called physical fractionation. As the fallout cloud is transported through the atmosphere, the early-forming particles with refractory radionuclides reach sufficient mass to fall from the debris cloud, while the lighter and less dense debris and volatile radionuclides will be transported further from the location of the explosion, a.k.a., ground zero.

As these fractionation processes occur, the radionuclides continue to transition from one element to another as they beta-minus decay through their respective mass chains toward stability. For this reason, refractory and volatile radionuclides are more often considered in their

mass chains instead of individually, and not all of them have condensation temperatures clearly above or below the soil solidification temperature. These mass chains and their respective categories identified by Hicks are given in Table 2.1. [25]

Table 2.1 Fractionation categorization of mass chains.

Mass Chains	Categorization
75-90 and 101-139	Volatile
92-100 and 142-180	Refractory
91, 140, 141	Mixed

To summarize, all fission products produced in the fireball will decay and condense as the fireball expands and cools with time. The timing will dictate when the fission product mass-chains decay, and the debris cloud materials and temperature will dictate when and how the fission products diffuse through or condense on other debris particles.

CHAPTER 3: MODELING AND MACHINE LEARNING METHODS

3.1 Modeling of Fallout Fractionation

For this research, surrogate models of the Korts and Norman (KN) fractionation model implemented in DELFIC were used. [20] Surrogate models enable uncertainties in the thermodynamic parameters governing fractionation to be propagated onto the KN model's predictions of fallout composition. Supervised machine learning classification tools were applied to the predicted fallout composition to identify combinations of fission products that classify explosive type even when the uncertainties in the thermodynamic parameters are large.

3.1.1 DELFIC Inputs and Modules

This research seeks to classify explosive type using the fission product activity per unit mass of fallout. Four types of explosives were analyzed. They are listed by fissile material and neutron spectrum listed in Table 3.1.

Table 3.1 Explosive types considered in this study.

Label	Fissile Material	Neutron Spectrum
u235fi	U-235	Fission
u235he	U-235	Fusion
p239fi	Pu-239	Fission
p239he	Pu-239	Fusion

Other inputs to DELFIC include explosive yield, burst height, wind velocity, and ambient temperature. DELFIC calculates the position and time-dependent distribution of fallout using three modules:

- The Initialization and Cloud Rise Module (ICRM) models the initial explosion (vaporization of materials and fission product generation) and the rise and stabilization of the fireball/debris cloud.
- The Diffusive Transport Module (DTM) models the cloud dynamics and the transport of fallout particles to the ground given atmospheric conditions, distributed versus particle size.
- The Output Processor Module (OPM) maps characteristics of the fallout field by position on the ground and by time since detonation. It tabulates the fallout composition, mass, and dose rate.

Sampling by rejection was used to select fallout collection that kept the dose rate to less than 1 R/hr and maintain a minimum fallout density of 100 mg/m^2.

3.1.2 DELFIC Implementation of the Korts and Norman (KN) Model

The original model implemented in DELFIC used the Freiling radial distribution model based on the lognormal distribution of fallout particle size observed from atmospheric testing and fallout collection. [26] This was later improved in the late 60's by Seery, who (using additional atmospheric nuclear testing data) observed that Freiling's model broke down for fallout particles larger than about 50 μm. [27].

Advancements in computing power enabled Korts and Norman to develop and implement physical models of the thermodynamic processes controlling fallout formation: condensation and diffusion. The KN model uses Henry's law to model the condensation of fission products onto particles in the debris cloud, and it uses the diffusion equation to model fission product penetration into debris particles.

The KN model uses a time-and temperature-dependent step process to simulate the condensation and diffusion of fission products. The change in temperature (ΔT) is held constant for each step, which produces increasingly longer time steps as the debris cloud expands and cools. This is illustrated in Figure 3.1. Before the beginning of the sequential temperature/time steps, blast physics dominate particle motion in the debris cloud. After a short time (a few seconds), the fission products are assumed to be initially uniformly distributed volumetrically throughout the cloud at a uniform temperature before condensation begins. This implicitly assumes condensation rates are uniform throughout the cloud.

Temperature is treated as constant during a given time step when diffusion is calculated, such that the temperature-dependent parameters of volume, surface concentration, diffusion, and Henry's Law coefficients are treated as constant during each diffusion step. At the end of the time step an instantaneous temperature drop ΔT is modeled.

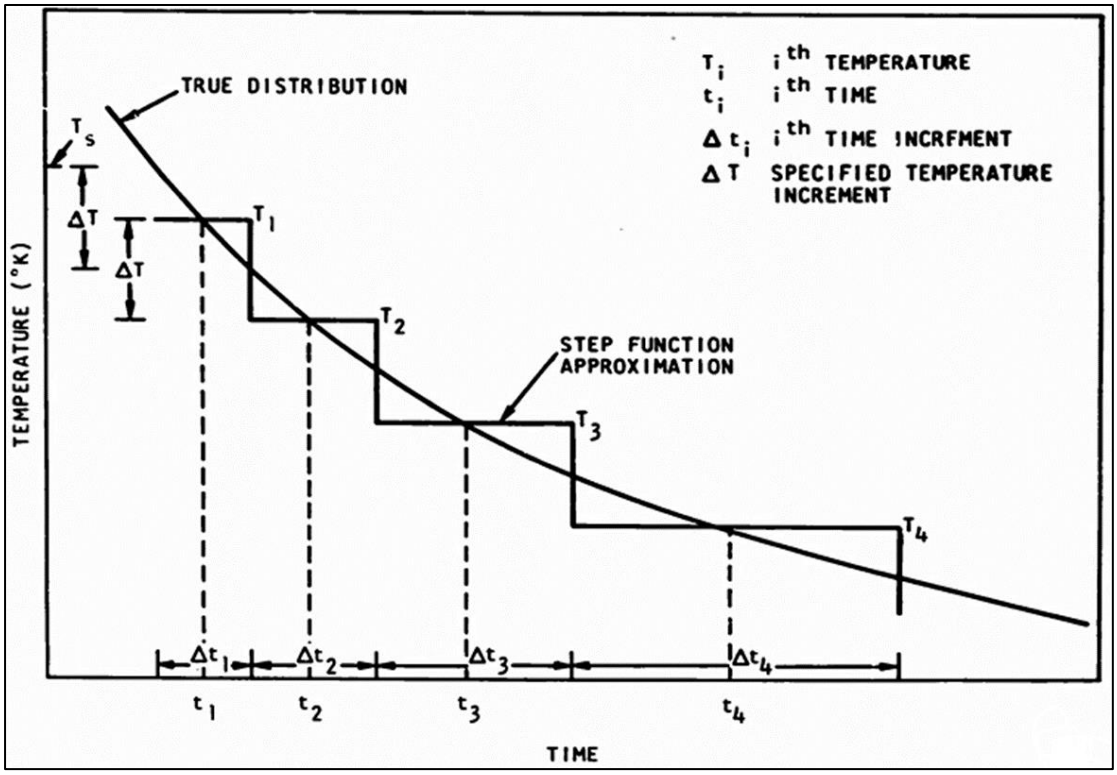

Figure 3.1 Graphical representation of the KN model time-temperature step process. **[13]**

For each temperature step, condensation and radioactive decay are calculated. Only a single radioactive decay is calculated at the completion of each time step. This simplification can introduce some error at short times immediately following the explosion, but these errors have negligible impact on fallout composition for realistic collection times, which are generally 24 hours or longer post-detonation. [13]

Other computational simplifications in the DELFIC implementation of the KN model are that fallout particles represented as spherical, glassy silicate particles that do not agglomerate. In practice however, irregular particles exhibiting agglomeration can be separated out during fallout collection. The fallout particles also follow the Frieling lognormal size distribution in the KN model. Gifford offers a detailed treatment of the equations governing Henry's law, diffusion, and their implementation in DELFIC. [20]

The two thermodynamic coefficients employed in the KN model are the Henry's law coefficient K_H, and the diffusion coefficient δ. Both exhibit temperature dependence following the law of Arrhenius:

$$log_{10}(K_H) = H_1 - \frac{H_2}{T} \quad \textbf{(3.1)}$$

$$log_{10}(\delta) = D_1 - \frac{D_2}{T} \quad \textbf{(3.2)}$$

The Henry's law coefficient is the ratio of concentrations in the gas phase and liquid phase. The parameter H_1 is the logarithm of the Henry's law coefficient at infinite temperature. The diffusion coefficient is in units of area per unit time, and the parameter D_1 is the logarithm of the diffusion coefficient at infinite temperature. H_2 and D_2 have units K. T is the temperature in degrees K. These coefficients are specific to each element and, where possible, DELFIC's implementation uses Henry's law coefficients measured for oxide compounds at 1500 C and 1 atmosphere. Where no measurements were available, the coefficients were estimated using measurements of the closest element with similar volatility. [28] Incomplete knowledge of the thermodynamic coefficients introduces large, unquantified uncertainties in the model. Figure 3.2 shows the elements that have measured Henry's Law coefficients highlighted in green. The estimated coefficients highlighted in red include the element used to estimate the coefficients in brackets. None of the measurements reported uncertainties.

Figure 3.3 shows the elements that have measured diffusion coefficients outlined in red. For elements lacking measured diffusion coefficients, DELFIC uses values estimated from a compensation law relationship demonstrated by Winchell and shown in the figure as grey. [29] [20]

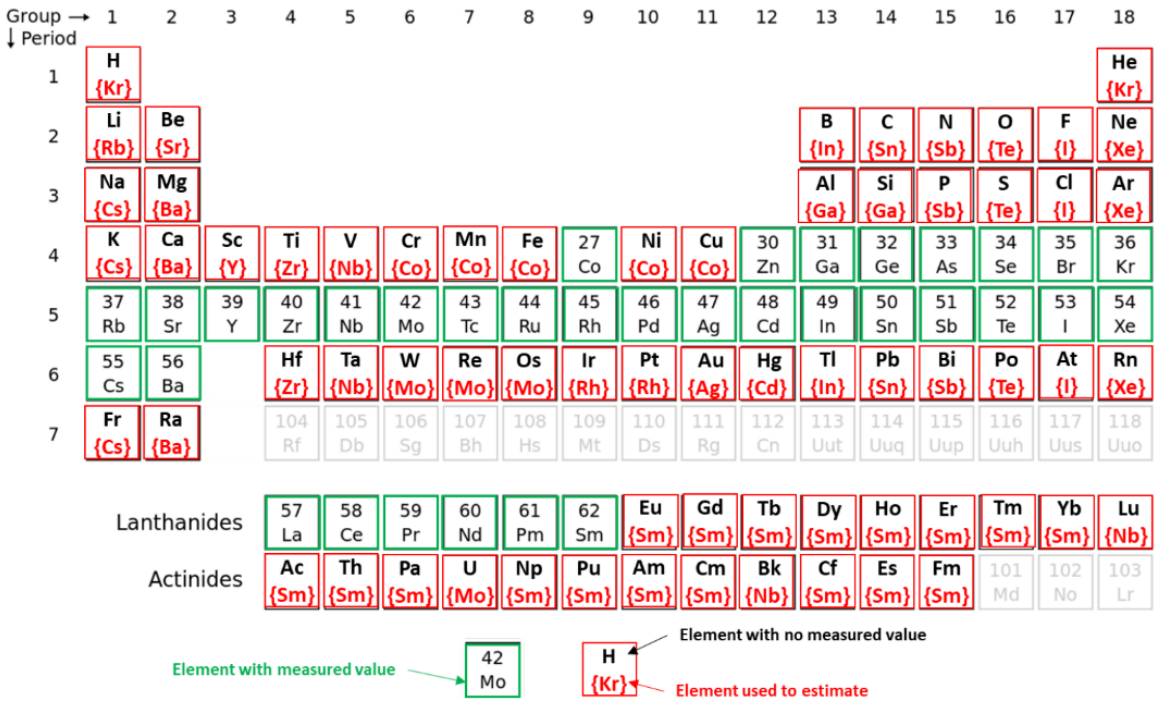

Figure 3.3 Periodic table depicting elements with measured (green) and estimated (red) Henry's law coefficients. **[20]**

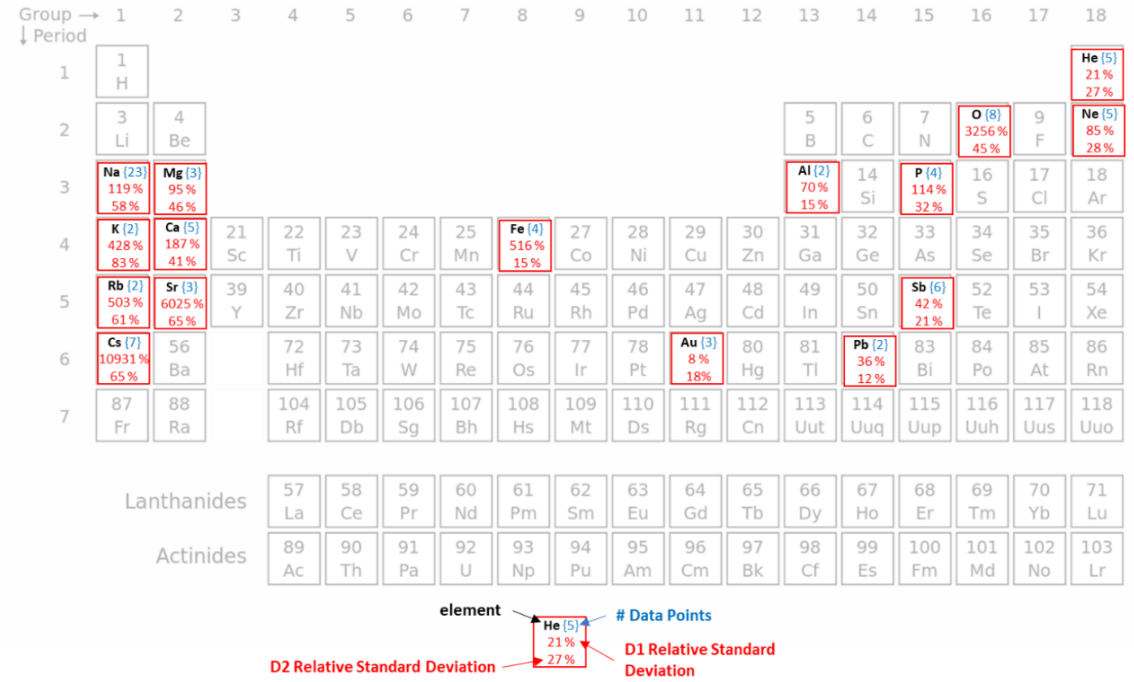

Figure 3.2 Periodic table depicting elements with measured (red) and estimated (grey) diffusion coefficients. **[20]**

The blue numbers in the Figure 3.3 indicate the number of measurements made for each element's diffusion coefficient. The relative standard deviations of those measurements are displayed in red in the bottom half of the squares. These deviations range from 8% to over 10,000%, and they can be attributed to variations in the conditions of the different experiments. In the extreme conditions of a fireball, the value of these coefficients and their uncertainties have only been roughly estimated.

These thermodynamic coefficients form the basis for fission product condensation on and diffusion through debris particles in the KN model. This research seeks to identify combinations of fission products that can classify explosive type even when predictions of their composition have large uncertainties in their thermodynamic coefficients.

3.1.3 Fallout Features Analyzed

The fallout property, or feature, analyzed in this thesis is fission product activity per unit mass of fallout. Gifford demonstrated that this metric reduces variance due to the randomized selection of fallout collection location. [20] The fallout collection particle size for this analysis was also constrained to 490-510 μm following Lucero's and Gifford's work. Lucero demonstrated that constraining particle size reduced fallout composition variance due to variations in wind velocity, explosive yield, and burst height. [19] Gifford confirmed the same observation for other size ranges including 270-279 μm and 730-750 μm. [20]

DELFIC predicts the activity of 355 different radionuclides in fallout particles, and Gifford analyzed those activities with thermodynamic coefficients uniformly sampled over ±50% of the coefficients' nominal values. Radionuclides that exhibited low activity (below 1,000 Bq/g) were excluded from further analysis. Gifford identified roughly a dozen fission products that

exhibited separation in activity by explosive type, making them potentially useful for explosive type classification. Figure 3.4 illustrates the qualitative utility of four different fission products for fission product classification. Eu-156 exhibits separation by explosive type in (a). Ag-111 and Ce-143 exhibit some overlap in (b) and (c). Cr-51 shows no promise for classification in (d).

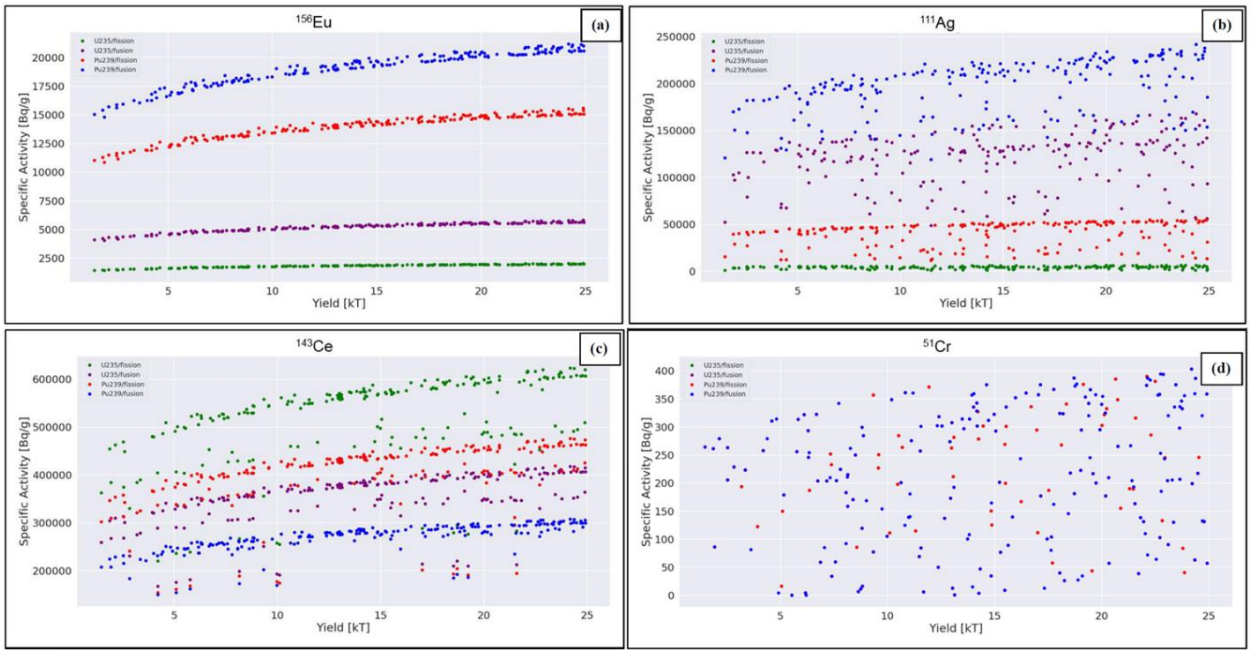

Figure 3.4 Visual separation of four different fission products by explosive type. **[20]**

Visual examination enabled Gifford to identify fission products that exhibited separation by explosive type even with large uncertainties in the thermodynamic parameters. Fission products like Eu-156 and Ag-111 shown in Figure 3.4 (a) and (b) that exhibit little to no overlap between explosive types are useful for classification. In contrast, the other two nuclides shown in Figure 3.4 (c) and (d) exhibit overlap for multiple explosive types. Though the Cr-51 appears to be useful for identifying Pu-239 as the fuel, note the low activity.

Using visual examination, 12 fission products exhibited potential to classify explosive type. These 12 fission products are listed in Table 3.2, they are separated by their fractionation category, i.e., volatile versus refractory.

Table 3.2 Fission products used in this study, listed by fractionation category.

Volatile	Refractory
As-77	Zr-95
Ag-111	Nb-95
Ag-112	Nd-147
Pd-112	Pm-151
Cd-115	Sm-153
In-115m	Eu-156

3.1.4 Sensitivity Analysis, Reduced-Order Modeling, and Surrogate Modeling

The KN model formally has several hundred parameters: for each element, there are two parameters each dictating the Henry's law and diffusion coefficient, respectively. The computational expense of propagating uncertainties through direct sampling on a model with hundreds of parameters is high. Gifford quantified the effects of thermodynamic parameter uncertainties on predicted fallout composition using global sensitivity analysis. [20] Identifying the most influential parameters can reduce the computational expense. Only the uncertainties in the influential parameters need to be propagated. Gifford used Morris screening for sensitivity analysis, which showed that of hundreds of parameters, less than 50 were influential.

Active subspace decomposition (ASD) identifies the subspace of model parameters spanned by mutually orthogonal eigenvectors composed of linear combinations of the parameters. The eigenvectors composed of parameters with the most influence on model

variance have corresponding eigenvalues with the largest magnitudes. Gifford found the most influential two eigenvectors for each fission product accounted for nearly 100% of the variance in activity. [20]

A surrogate model trained on those eigenvectors was used to calculate the activity of fission products using only four dimensions: the two active subspace dimensions, the explosive yield, and the burst height. Wind velocity, particle size range, and sample collection time were held constant throughout. Table 3.3 lists the variables and constants with their range or values except for the two thermodynamic eigenvectors which are specific to each fission product element. Gaussian process regression (GPR) surrogate models trained on the ASD eigenvectors, explosive yield, and burst height for 2,000 DELFIC simulations were used to synthesize realizations of fallout composition for random variations in the thermodynamic parameters. [20] The GPR models ran ~ 100,000 times faster than the KN model, which enabled ~ 100,000 realizations of fallout composition to be synthesized in the time required for one prediction using the original KN model. [30]

Table 3.3 Non-thermodynamic variables and constants with their categories, ranges, or values used to produce the data for this research.

Variables	**Categories or Range**
Fuel	U-235 or Pu-239
Neutron Spectrum	Fission, Fusion
Explosive Yield	0 – 25 kilotons TNT equivalent (uniformly sampled)
Burst Height	0 – 25 meters (uniformly sampled)
Constants	**Values**
Wind Velocity	5 meters/second constant speed and direction
Sample Timing	5 days post-detonation
Sample Particle Size	490 – 510 μm

3.1.5 Calculations of Fallout Composition

For this research, 200,000 realizations of fallout composition were synthesized using the surrogate model for each of the 4 explosive types and 12 fission products, with randomly sampled explosive yield and burst height. Burst height and explosive yield were correlated across all 12 fission products for a given realization. The thermodynamic coefficients of individual fission products were randomized with a uniform distribution over ±50% of nominal values (i.e., within ± 50% tolerance).

Since Zr-95 undergoes beta-minus decay to Nb-95 100% of the time, the data for a pairwise activity plot would ideally lie in a straight line, however, independent randomization of the thermodynamic parameters induces the variance observable in Figure 3.5 (a). A plot of Eu-156 vs. Zr-95 is given in Figure 3.5 (b) exhibiting correlation from explosion realizations but greater explosive type activity separations due to their different mass chains.

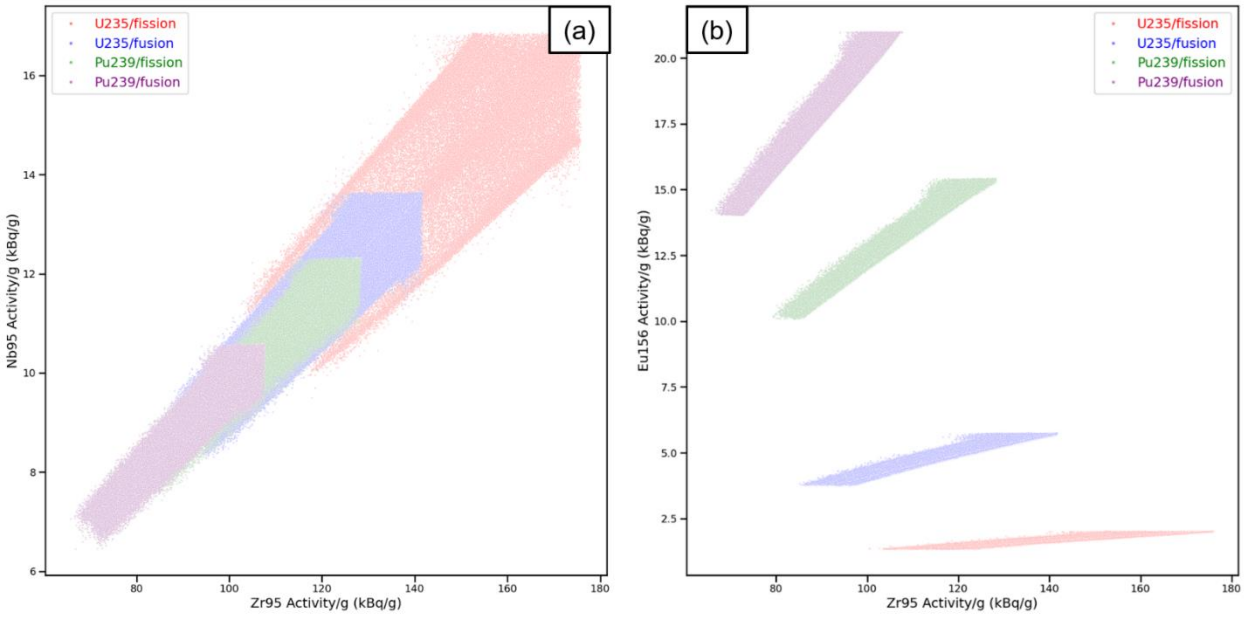

Figure 3.5 Activity of Nb-95 vs. Zr-95 (a) and Eu-156 vs. Zr-95 (b)

3.2 Supervised Machine Learning

Supervised machine learning is a subset of the larger machine learning field. Machine learning empowers machines to analyze data, build models, and construct predictions without explicit programming. [31] The term “supervised” indicates that the machine is trained on a fully labeled data set (training set) of inputs and outputs to produce a predictive model. The trained model can generate predictions from new inputs. Supervision also allows the user to adjust the algorithms, select features, and structure data to optimize model predictive capability for new input data. If a model exhibits significant bias, the model is likely too simple and overgeneralized. If a model exhibits significant variance, it is likely overfit and imprecise when tested. Figure 3.6 illustrates bias, variance, underfitting, and overfitting. Machine learning algorithms attempt to minimize bias and variance and produce models that are both accurate and precise. To this end, the models are tested against separate set (testing set) of known inputs and outputs to evaluate predictive accuracy once the model has been trained.

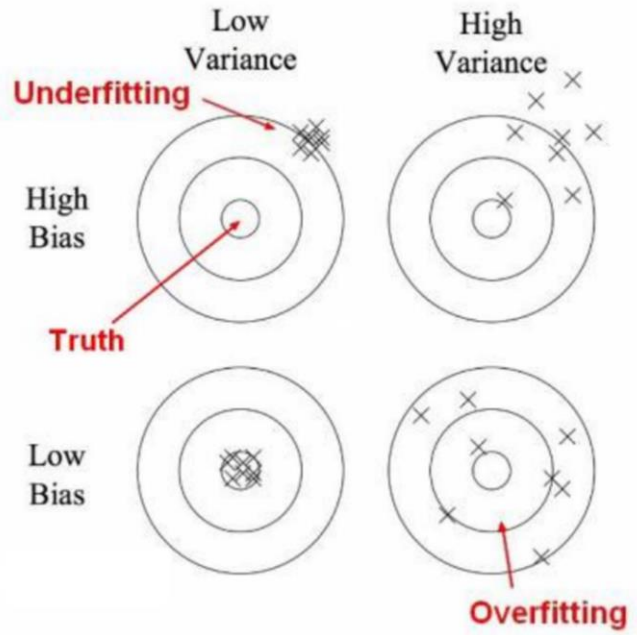

Figure 3.6 Diagram illustrating model bias and variance. **[49]**

Supervised machine learning methods are grouped into regression or classification methods depending on the output type. [32] Regression methods are used to predict continuous outputs such as temperature, distance, or mass. Classification methods are used to categorize outputs such as specific entities (people, organizations, products), a limited set of integers or levels, or in the case of this research: explosive type.

To demonstrate some basic regression concepts, consider the datapoints listed in Table 3.4. These datapoints are generated from the sine-polynomial function within the domain given in Equation 3.3. Assume that Equation 3.3 is not known - only the datapoints in the table are - and a model is desired to predict *f* given q. Since the output is a continuous value, regression methods can be used to build the model.

$$f(q) = (6q^2 + 3)\sin(6q - 4)\,,\ for\ q \in [0, 2] \qquad \textbf{(3.3)}$$

Table 3.4 Data derived from the sine-polynomial function Equation 3.3

q	0.03	0.17	0.38	0.52	0.63	0.72	0.87	0.94
f(q)	1.89	-0.51	-3.82	-3.56	-1.17	1.92	7.08	8.28
q	1.12	1.3	1.4	1.5	1.66	1.83	1.9	
f(q)	4.31	-8.04	-14.05	-15.82	-6.20	14.82	22.16	

Multiple linear regression can be used to model this data, in this case resulting in an 8th degree polynomial shown in Figure 3.6. The model given by the red line achieves a good fit to the true but "unknown" analytic solution given by the black line. The data points are given in blue. If we expand the domain of the independent variable to $q \in$ [-0.5, 2.5] as shown in Figure 3.6 (b), we see that predictions outside the training domain diverge from the analytic solution. To

improve this model beyond the original training domain, additional data over the expanded domain is required to re-train it. The quality of the model will reflect the quality of the data used to train it, and extrapolating responses beyond the training domain is ill-advised. A different type of model could also be selected if additional training data outside of the original domain is not obtainable.

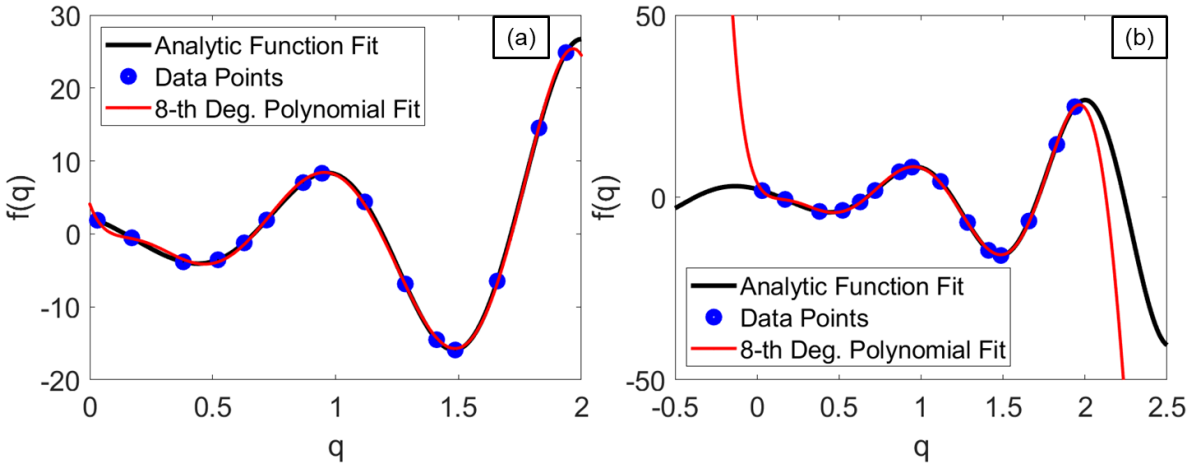

Figure 3.7 Sine-polynomial function with 8th degree polynomial fit within range (a) and expanded beyond range (b)

Figure 3.7 shows a Gaussian process regression (GPR) model applied to the same data. GPR models predict an expected output and uncertainty within and outside the training domain. This model, while imprecise beyond the training domain, shows improved predictive accuracy relative to the 8th degree polynomial model.

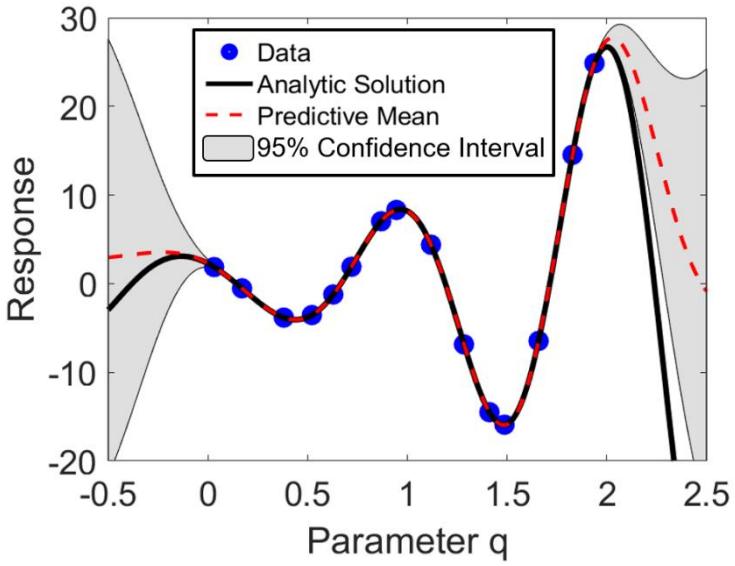

Figure 3.8 A Gaussian process regression fit to the data given in Table 3.4.

Classification algorithms in machine learning seek to identify a class for given input. A model is trained with known data and tested against another known set for accuracy. Many machine learning algorithms employ hyperparameters or learning model configurations that can be optimized given a dataset's size, complexity, and variance.

For this thesis, decision tree, random forest, and gradient boosting classification was used to identify explosive type given the predicted activity of 12 fission products. Explosive yield and burst height were withheld from the training data for classification; they would be unknown (or poorly known) in a real explosion. The full dataset described in 3.1.5 was randomly split with 70% used to train models and 30% reserved to test the model accuracy.

3.2.1 Decision Tree Classifiers

Decision tree classifiers use a set of if-then rules called binary recursive partitioning to classify input data. Each new rule or partition is exclusive and exhaustive for classifying the

entire remaining dataset. The input data can be continuous or discrete. Generally, decision tree algorithms are based on the concept of information gain. [33]

Information gain is evaluated for each variable. The variables with the highest information gain are those that offer the greatest reduction in information entropy *E*. Entropy is defined in Equation 3.4, with *C* being the number of classes and p_i the proportion of the dataset consisting of class *i*.

$$E = -\sum_i^C p_i \log_2 p_i \quad \textbf{(3.4)}$$

Information gain is then evaluated to determine the quality of a split in the data using Equation 3.5, where E_p is the entropy of the parent dataset and E_d is the weighted average of the daughter datasets after the split. The algorithm tests many variables and split locations. The variable and split with the highest information gain is selected as a decision node in the tree. If variables offer identical information gain, the first one in the sequence is selected.

$$Gain = E_p - E_d \quad \textbf{(3.5)}$$

The algorithm will iterate through subsequent decision nodes based on the information splits above it until there is no more information that can be gained by further splitting. Decision nodes, when displayed as a chart, resemble an inverted tree with the first rule being the root node. Terminal nodes are called leaf nodes. See Figure 3.9 for an example of a labeled decision tree developed in this research to classify explosive type.

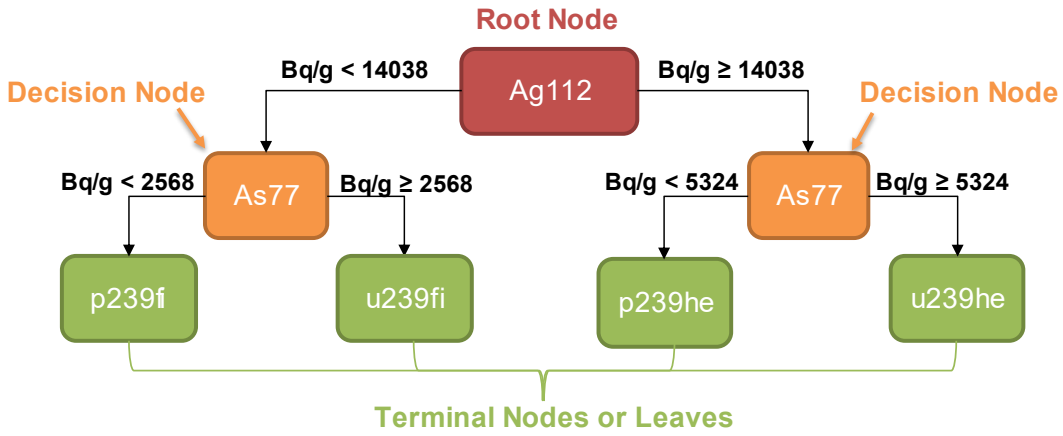

Figure 3.9 Decision tree showing the root node, two decision nodes, and four terminal or leaf nodes using activity levels of Ag-112 and As-77 to classify explosive type.

In Figure 3.9, the root node designates Ag-112 as the fission product with highest information gain. An activity of about 14 kBq/g was the optimal dividing line between neutron spectra. If an explosion produces Ag-112 with more than 14 kBq activity per gram of fallout, it has a harder energy spectrum characteristic of a more sophisticated, fusion boosted explosive. Divisions occur on each side at the middle level of the tree, with As-77 activity determining if the explosive was fueled by Pu-239 or U-235. These divisions and their levels given in the decision tree are illustrated by the plot shown in Figure 3.10. In this case, the decision tree can identify explosive type with no misclassifications, even with no knowledge of explosive yield or burst height, and with ±50% tolerance in the thermodynamic parameters governing fractionation.

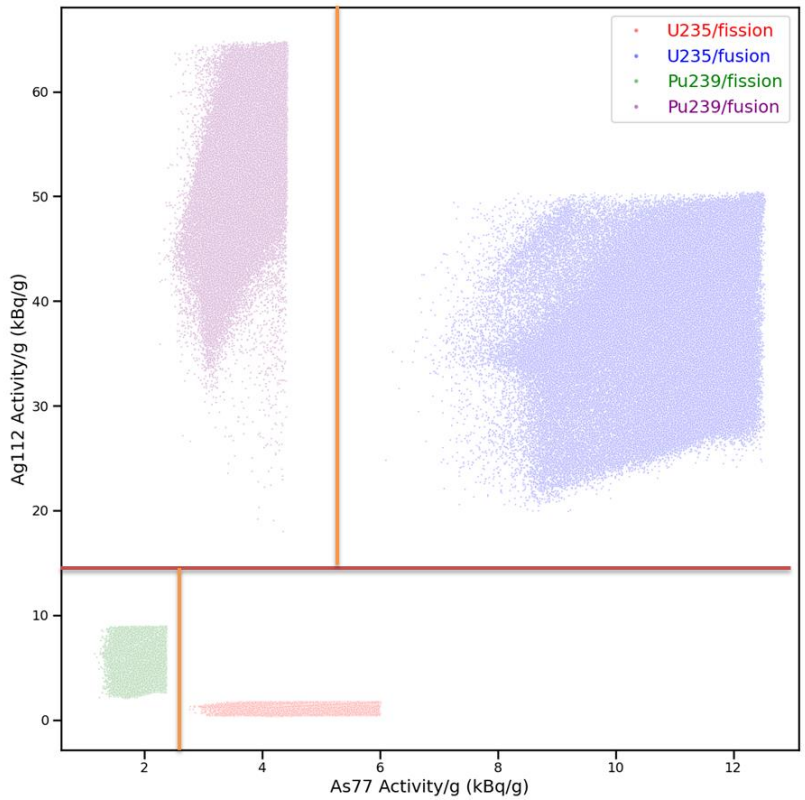

Figure 3.10 Ag-112 vs. As-77 activity with root (red) and decision node dividers (orange) displayed.

Decision trees can be intuitive to interpret and communicate. Techniques, like decision tree pruning, streamline larger tree models by reducing the number of leaves and/or nodes. Tree pruning improves tree simplicity with minimal increase in prediction error.

Some data are less conducive to decision tree modeling and create sprawling, complex trees that result in overfitting of the data (high variance). Figure 3.11 illustrates a well-fit decision tree (a) vs. decision tree overfit (b). The model for (b) would likely perform poorly given new test data of the same type. Overfitting was not observed in this research involving decision tree training and testing because the dataset was larger (200,000 realizations per explosive type) it lacked large outliers, and the decision tree algorithm had a tree growth depth limit. [34]

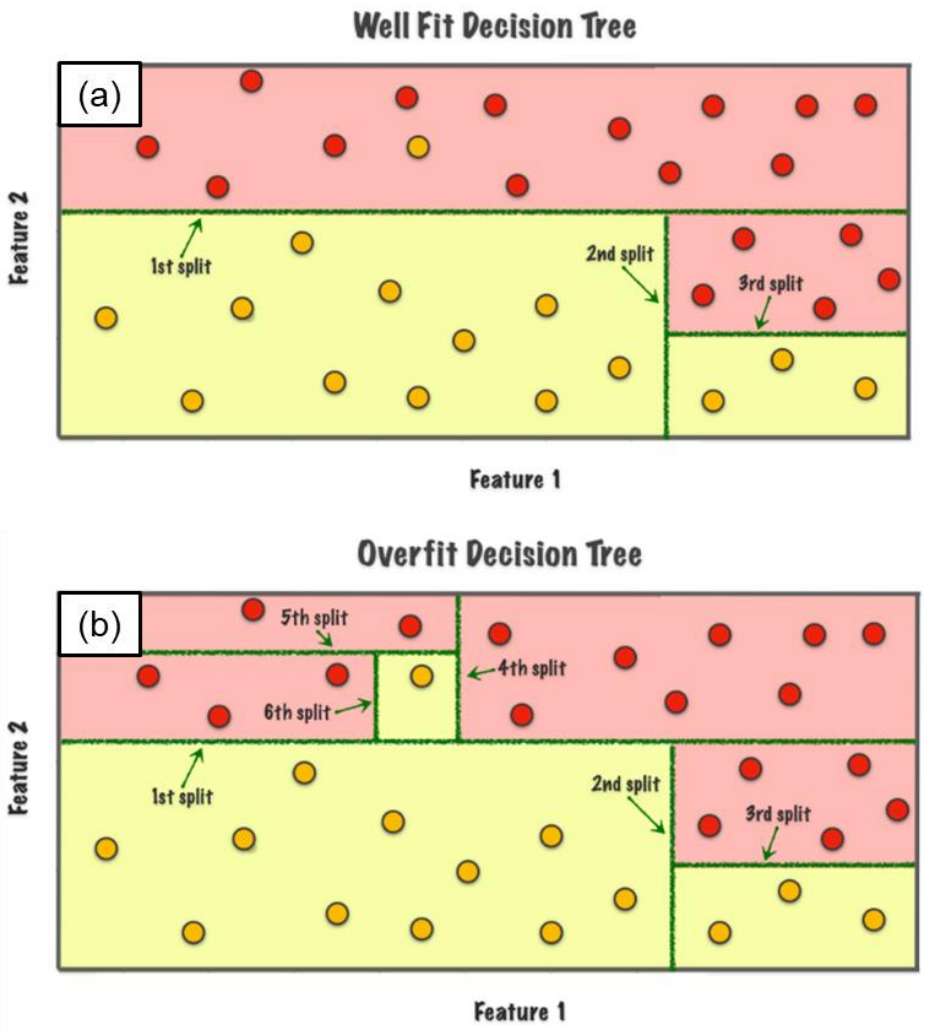

Figure 3.11 Examples of well fit (a) and overfit (b) decision trees. **[50]**

The hierarchical nature of decision trees can make them unstable when deciding between many variables of similar information gain. A small change in training data can result in very different tree patterns. For example, Dwyer and Holte demonstrated that by adding a single datapoint to a training set of 106 realizations for lymphography data, the tree changed so drastically that only a single leaf maintained the same decision rules. [35] Figure 3.12 shows the two resulting decision trees. In such cases, other forms of modeling should be considered.

Instability was not identified in the decision trees in this research. Altering training set sizes and seed number produced some variation (<5%) in activity levels for decision nodes, but tree structures and their selected features were unchanged.

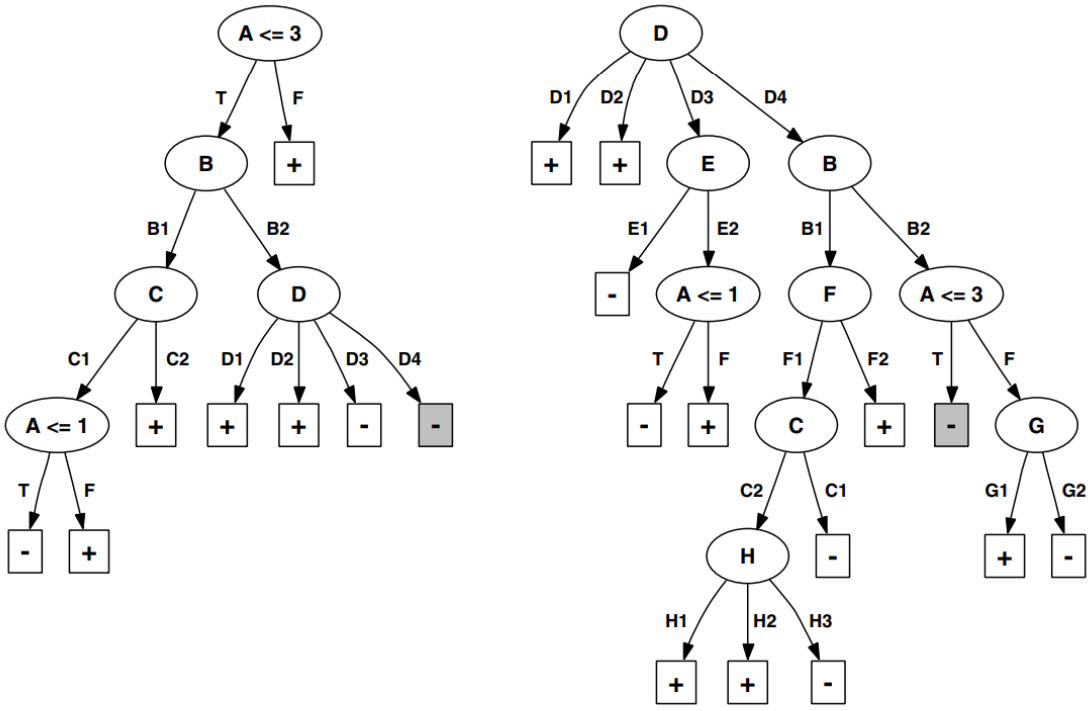

(a) Tree grown from 106 examples (b) Tree grown from 107 examples

Figure 3.12 Example illustrating decision tree instability from slight modification to a lymphography data training set. The shaded leaf is the only one where the same decision tests are performed. **[35]**

3.2.2 Random Forest Classifiers

Random forest classifiers take the average of multiple independent decision trees to reduce overfitting (high variance). They employ two techniques: (1) bootstrap aggregating or "bagging", and (2) random feature selection. [36] [37]

Bootstrapping creates variants of the training dataset by uniformly sampling with replacement. Bagging creates decision trees for the bootstrapped datasets and predicts class

based on the majority predictions of the many trees. This reduces the variance experienced with single decision trees without increasing bias.

Bootstrapping is also applied to features, randomly selecting a subset of features from a user-defined number. For example, from the 12 fission products of interest, a random set of 5 could be used to create a decision tree. Additional trees with a new randomly selected group of 5 radionuclides would then be constructed. This random feature selection reduces correlation when a dataset has one or two highly influential features and reduces variance in the model without increasing bias.

Random forest classifiers have reported significant performance improvements over decision trees for certain datasets because of their ability to generalize trends and reduce overfit of training data. [37] In this research, most cases that exhibited test error in decision tree classification showed improvement using random forest classification. In most cases, the error reductions were substantial (>50% of total remaining error). In a few cases, error was reduced to zero, and in a very few cases, error marginally increased. Figure 3.13 shows an example of Sm-153 vs. Zr-95 with decision tree rules partitioning the graph. The limited binary splitting rules of decision trees, shown as the horizontal and vertical lines, resulted in 0.55% test misclassification error. Random forest classification was able to reduce test error to zero. However, the random forest model is also less interpretable, as classification comes from a “forest” of independent decision trees and not just one. As such, it can offer no simple graphical depictions like single decision trees can.

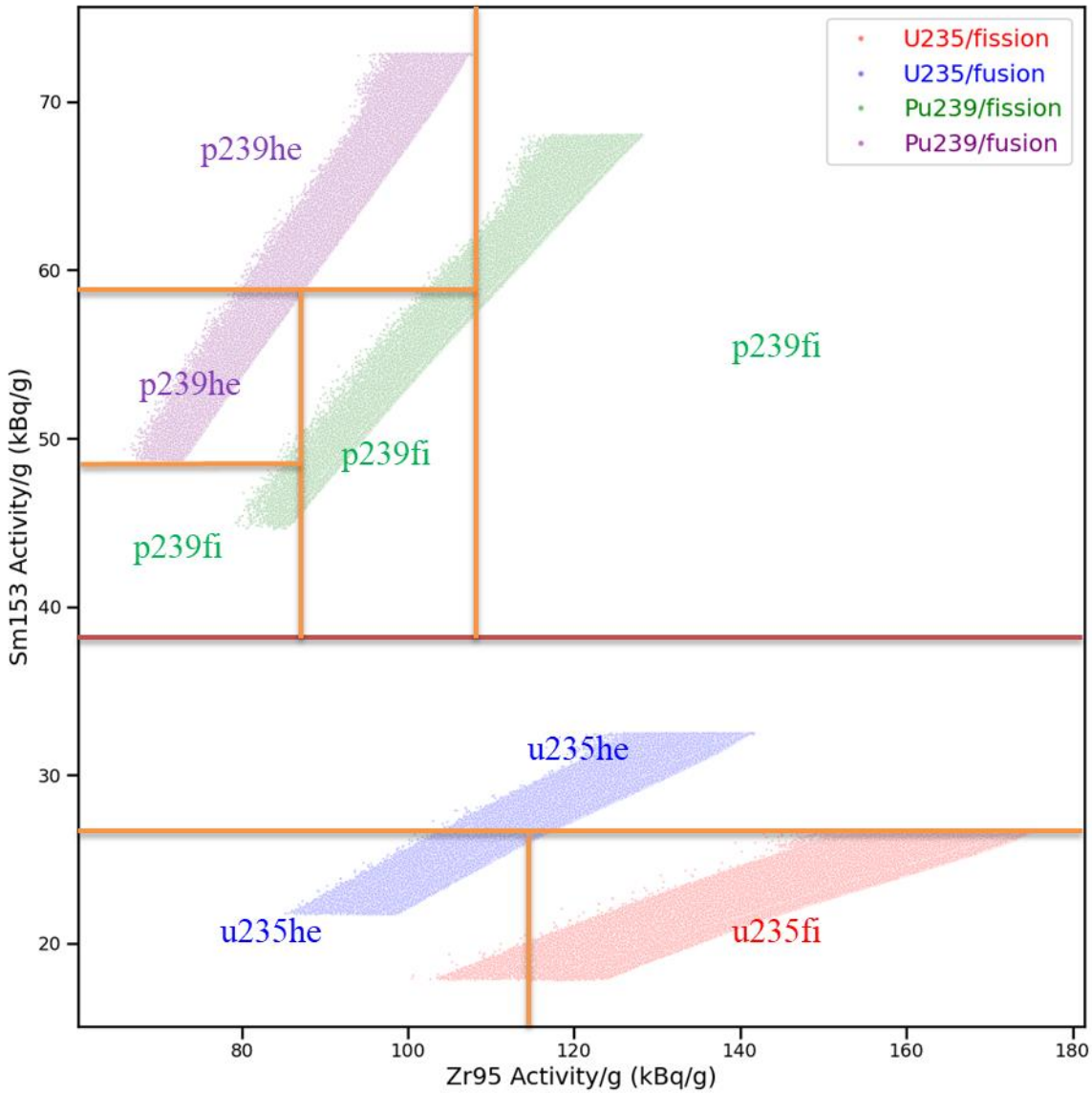

Figure 3.13 Sm-153 vs. Zr-95 activity with decision tree nodes and classifications displayed. Unlike decision tree learning, random forest learning classified this pairing with zero error.

3.2.3 Gradient Boosting

Gradient Boosting is another decision tree technique that uses a forest of decision trees to make predictions. Distinctively, it grows truncated decision trees called stumps or weak learners and each stump influences the next by giving higher weighting to misclassified data than correctly classified data. These truncated and weighted trees accumulate additively, taking small

steps in the correct direction to keep variance low. The completed additive forest is used to predict the result. Several hyperparameters must be optimized for this model to reduce error and avoid overfitting, including tree depth (how many decision nodes to allow), shrinkage (learning rate step-size), number of observations in terminal nodes, number of trees to fit, and interaction depth (1 for an additive model, 2 for 2-way interactions, etc.). Tuning hyperparameters on boosted models can result in long run times, but it can reduce variance over random forest models for many datasets. [38] [39]

In this research, gradient boosting provided no notable improvement over random forest classification. Each gradient boosting run required significant time for model tuning and training. This method better lends itself to different datasets or to applications where small improvements of models are worth a large time investment.

3.2.4 Classifier Selection

There are many other classification methods not explored here, with more still under development. There is no universal guide for method selection that can rank order them for effectiveness. In machine learning, the "no free lunch" theorem states that, "averaged over all possible data-generating distributions, every classification algorithm results in the same error rate on data outside the training set. In other words, there is no learning algorithm that is universally optimal." [36] Given a priori knowledge of the dataset's characteristics (range, distribution, variance, etc.), one may be able to identify several effective methods. Best practice is to apply several different methods and compare results. Among methods that do not require long run times, boosted trees, random forests, and bagged decision trees regularly perform well for most data sets. [40] If interpretability of a model is paramount, using more advanced methods can

assist in feature selection and reduce the data to a subset of influential features. Simple decision trees can be trained on the feature subset and evaluated for accuracy and variance, potentially producing an interpretable and sufficiently accurate model.

CHAPTER 4: RESULTS AND DISCUSSION

4.1 Data Preprocessing

The data produced in Section 3.1.5 were analyzed with the statistical learning language R. [41] [42] Table 4.1 shows data from the first realization of each explosive type. As stated in Section 3.1.5, outputs of individual realizations of fission product activity are correlated only by explosive type, explosive yield, and burst height. There were 200,000 simulated realizations for each of the four explosive types. The dataset was divided into a training set of 560,000 (70%) realizations and a test set of 240,000 (30%) realizations.

Table 4.1 Sample of input data for supervised machine learning.

Realization	**Explosive Type**	**Nuclide and Activity (kBq/g)**					
1	**U235 Fission**	**As-77:** 4.38	**Zr-95:** 121.78	**Nb-95** 11.66	**Ag-111:** 3.63	**Pd-112:** 1.05	**Ag-112:** 1.18
		Cd-115: 4.09	**In-115m:** 4.39	**Nd-147:** 180.71	**Pm-151:** 23.88	**Sm-153:** 18.38	**Eu-156:** 1.39
200,001	**U235 Fusion**	**As-77:** 11.03	**Zr-95:** 124.81	**Nb-95** 12.05	**Ag-111:** 125.21	**Pd-112:** 32.65	**Ag-112:** 35.18
		Cd-115: 100.18	**In-115m:** 73.23	**Nd-147:** 175.23	**Pm-151:** 26.41	**Sm-153:** 28.58	**Eu-156:** 5.07
400,001	**Pu239 Fission**	**As-77:** 1.74	**Zr-95:** 93.54	**Nb-95** 8.98	**Ag-111:** 40.53	**Pd-112:** 5.64	**Ag-112:** 6.61
		Cd-115: 10.11	**In-115m:** 10.97	**Nd-147:** 178.80	**Pm-151:** 48.25	**Sm-153:** 49.69	**Eu-156:** 11.26
600,001	**Pu239 Fusion**	**As-77:** 3.21	**Zr-95:** 77.17	**Nb-95** 7.65	**Ag-111:** 165.19	**Pd-112:** 39.77	**Ag-112:** 47.07
		Cd-115: 128.49	**In-115m:** 168.34	**Nd-147:** 151.61	**Pm-151:** 44.45	**Sm-153:** 52.65	**Eu-156:** 15.16

Figure 4.1 shows the mean activity of the 12 radionuclides across all realizations for each explosive type. The activity of a radionuclide plays a significant role in its observability by radiation detectors. Higher activity levels are typically more observable. Activity is not the only important factor in observability. Detector efficiency, gamma energies, and gamma intensities also impact observability.

Radionuclide activity was the factor used for this research, with the response being explosive type classification. Decision tree classifiers were able to determine several combinations of two fission products capable of classifying all test data with zero error, but the same might not be true if the dataset were developed by incorporating additional observability factors besides predicted activity. Because only predicted activity was used in this research as a metric, higher order combinations and additional machine learning classifiers were evaluated beyond the zero-error pairings from decision tree classification.

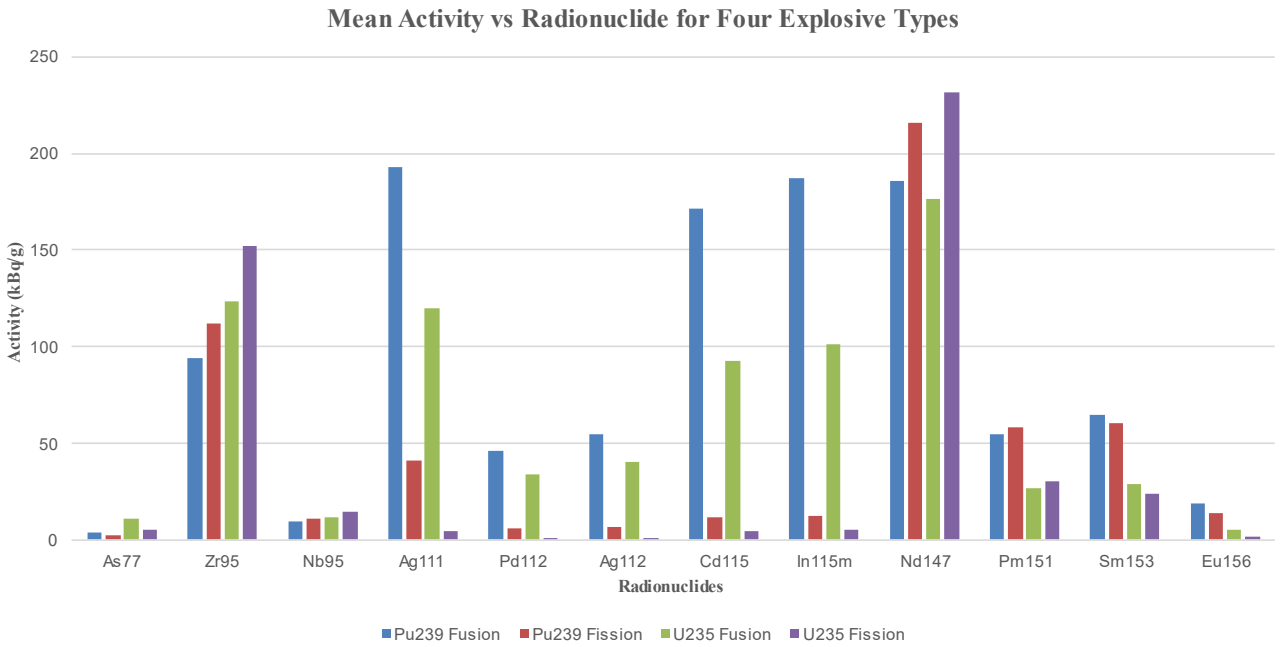

Figure 4.1 Mean activity levels for each radionuclide vs. explosive type.

4.2 Decision Tree Classification for Single Radionuclides

Individual radionuclides were analyzed using decision tree classification to determine explosive type. [34] This analysis indicated which radionuclides offer the higher information gains and therefore were more likely to be root nodes of decision trees with more than one radionuclide. Table 4.2 lists the results.

Table 4.2 Summarized decision tree classification results for individual radionuclides.

Nuclide	Terminal Nodes	Training Misclassification of 560,000	Training Misclassification Error Rate	Test Misclassification of 240,000	Test Misclassification Error Rate
As77	4	17,752	3.17%	7,577	3.16%
Zr95	5	156,507	27.95%	67,209	28%
Nb95	5	164,434	29.36%	70,627	29.42%
Ag111	5	27,542	4.92%	11,929	4.97%
Ag112	5	33,692	6.02%	14,751	6.15%
Pd112	5	34,014	6.07%	14,806	6.17%
Cd115	4	5,967	1.07%	2,633	1.1%
In115m	4	6,058	1.08%	2,578	1.07%
Nd147	5	231,393	41.32%	99,402	41.41%
Pm151	4	135,509	24.2%	57,858	24.1%
Sm153	4	119,840	21.4%	51,631	21.51%
Eu156	5	11,939	2.13%	5,187	2.16%

This analysis produced simple trees of only four or five terminal nodes, classifying the data with error rates ranging from about 1% to 41%. The radionuclides Cd-115 and In115m each produce a near 1% test error rate. Cd-115 decays into In-115m, and with the half-life of the

parent being greater than that of the daughter, the two radionuclides soon establish secular equilibrium. The mechanism is similar for Pd-112 → Ag-112 and Zr-95 → Nb-95, which is why each parent exhibits a classification performance rate similar to its daughter. Figure 4.2 graphically displays the decision tree for In-115m.

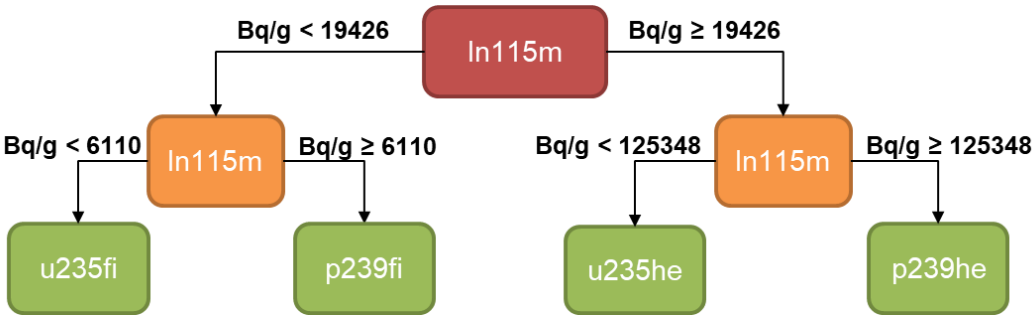

Figure 4.2 Decision tree for In-115m resulting in 1.07% misclassification rate.

Figures 4.3 and 4.4 show the activity of all 12 nuclides plotted against burst height and explosive yield respectively. The degree of separation by explosive type can be seen for each radionuclide. There is little variance in activity due to changing burst height for each radionuclide. However, there is higher variance in activity with changing yield, and there are distinct differences in the magnitude of variation from one radionuclide to another. Nd-147 is identified in Table 4.2 as having the lowest ability to classify explosive type, and in Figure 4.4 the reason for this is apparent from the large variance in activity versus yield. The best single classifiers, Cd-115 and In-115m, display some overlap between explosive types, but they appear relatively insensitive to changes in yield. Eu-156 exhibits separation between explosive types and relative insensitivity to yield.

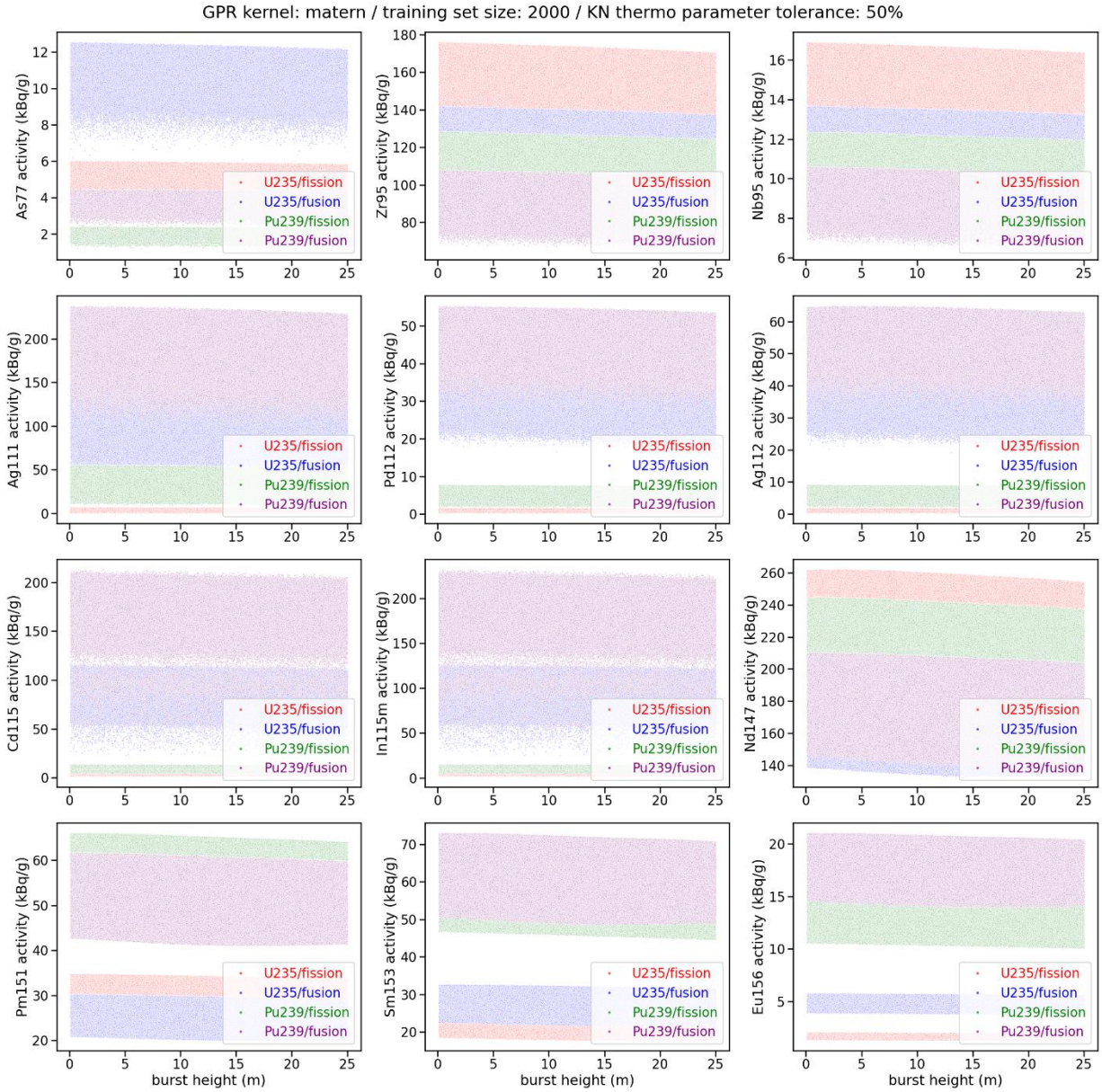

Figure 4.3 Activity of each radionuclide vs. burst height.

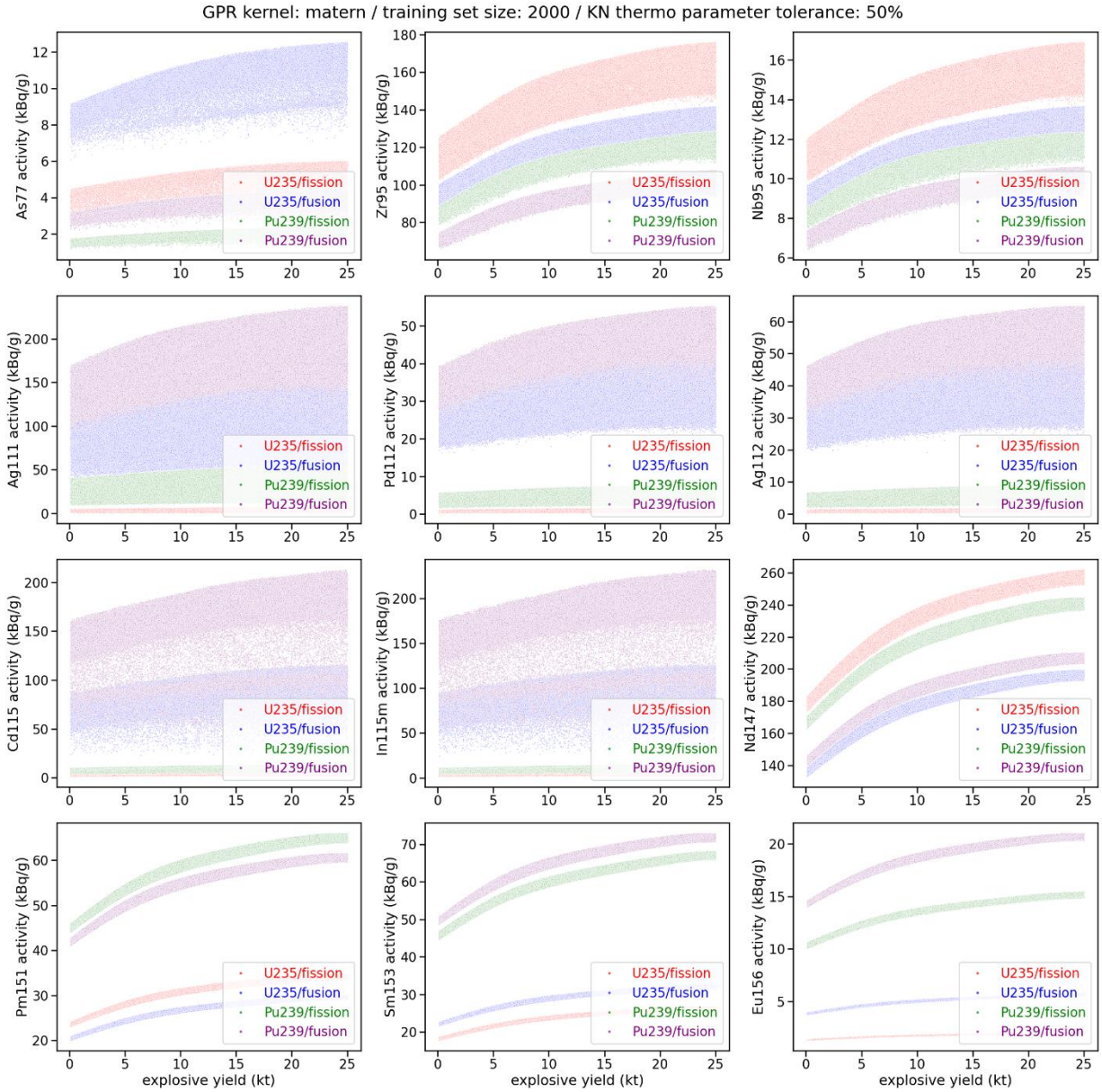

Figure 4.4 Activity of each radionuclide of interest vs. explosive yield.

4.3 Decision Tree Classification for Radionuclide Pairs

Combinations of two radionuclides were analyzed using the same algorithm described in the previous section. The results showed that 16 of 66 combinations could classify the test data with zero error. Of these zero-error combinations, no radionuclide had a mass number within 35

nucleons of the other. This makes intuitive sense, as combinations of light, heavy, and medium-mass fission products are complimentary for classification.

There were 46 of the 66 combinations that resulted in less than 1% test misclassification error, and only 3 combinations that resulted in misclassification error above 10%. Tables 4.3 and 4.4 present the results for each combination, fractionation category, number of terminal nodes, and training and testing misclassification error. These results indicate that decision tree classifiers can offer useful and interpretable models for classification of this data.

Table 4.3 Decision tree results, radionuclide pairs 1-33 of 66 ordered by minimal test error.

Combination	Fission Product 1	Fission Product 2	Fractionation Category	Mass Number Separation	Terminal Nodes	Training Misclassification Error Rate (of 560k)	Test Misclassification Error Rate (of 240k)
1	As-77	Ag-112	Both Volatile	35	4	0.0000%	0.0000%
2	As-77	Pd-112	Both Volatile	35	4	0.0000%	0.0000%
3	As-77	Cd-115	Both Volatile	38	4	0.0000%	0.0000%
4	As-77	In-115m	Both Volatile	38	4	0.0000%	0.0000%
5	Ag-112	Pm-151	Mixed	39	4	0.0000%	0.0000%
6	Ag-112	Sm-153	Mixed	41	4	0.0000%	0.0000%
7	Ag-112	Eu-156	Mixed	44	4	0.0000%	0.0000%
8	Pd-112	Pm-151	Mixed	39	4	0.0000%	0.0000%
9	Pd-112	Sm-153	Mixed	41	4	0.0000%	0.0000%
10	Pd-112	Eu-156	Mixed	44	4	0.0000%	0.0000%
11	Cd-115	Pm-151	Mixed	36	4	0.0000%	0.0000%
12	Cd-115	Sm-153	Mixed	38	4	0.0000%	0.0000%
13	Cd-115	Eu-156	Mixed	41	4	0.0000%	0.0000%
14	In-115m	Pm-151	Mixed	36	4	0.0000%	0.0000%
15	In-115m	Sm-153	Mixed	38	4	0.0000%	0.0000%
16	In-115m	Eu-156	Mixed	41	4	0.0000%	0.0000%
17	As-77	Pm-151	Mixed	74	4	0.0018%	0.0021%
18	As-77	Sm-153	Mixed	76	4	0.0018%	0.0021%
19	As-77	Eu-156	Mixed	79	4	0.0018%	0.0021%
20	Nd-147	Sm-153	Both Refractory	6	8	0.0018%	0.0038%
21	Nd-147	Eu-156	Both Refractory	9	5	0.0043%	0.0050%
22	Sm-153	Eu-156	Both Refractory	3	6	0.0043%	0.0050%
23	As-77	Ag-111	Both Volatile	34	5	0.0039%	0.0058%
24	Zr-95	Eu-156	Both Refractory	61	5	0.0045%	0.0071%
25	Nb-95	Eu-156	Both Refractory	61	5	0.0095%	0.0104%
26	Ag-111	Pm-151	Mixed	40	4	0.0000%	0.0171%
27	Ag-111	Sm-153	Mixed	42	4	0.0000%	0.0171%
28	Ag-111	Eu-156	Mixed	45	4	0.0000%	0.0171%
29	Pm-151	Sm-153	Both Refractory	2	11	0.0336%	0.0400%
30	As-77	Zr-95	Mixed	18	5	0.0559%	0.0517%
31	Nb-95	Pd-112	Mixed	17	6	0.1457%	0.1475%
32	As-77	Nb-95	Mixed	18	5	0.1139%	0.1550%
33	Cd-115	In-115m	Both Volatile	0	5	0.1746%	0.1779%

Table 4.4 Decision tree results, radionuclide pairs 33-66 ordered by minimal test error.

Combination	Fission Product 1	Fission Product 2	Fractionation Category	Mass Number Separation	Terminal Nodes	Training Misclassification Error Rate (of 560k)	Test Misclassification Error Rate (of 240k)
34	Ag-111	Cd-115	Both Volatile	4	5	0.1914%	0.1920%
35	Ag-111	In-115m	Both Volatile	4	5	0.1911%	0.2016%
36	Ag-112	In-115m	Both Volatile	3	5	0.2491%	0.2604%
37	Pd-112	In-115m	Both Volatile	3	5	0.2505%	0.2625%
38	Ag-112	Cd-115	Both Volatile	3	5	0.2534%	0.2738%
39	Pd-112	Cd-115	Both Volatile	3	5	0.2593%	0.2792%
40	Nb-95	Sm-153	Both Refractory	58	9	0.3211%	0.3337%
41	Pm-151	Eu-156	Both Refractory	5	5	0.3668%	0.3875%
42	Zr-95	Ag-112	Mixed	17	5	0.4975%	0.4975%
43	Zr-95	Pd-112	Mixed	17	5	0.4793%	0.5079%
44	Zr-95	Sm-153	Both Refractory	58	8	0.5454%	0.5541%
45	Nb-95	Ag-112	Mixed	17	5	0.6254%	0.6420%
46	Zr-95	Ag-111	Mixed	16	5	0.9161%	0.7958%
47	Nb-95	Ag-111	Mixed	16	5	0.9743%	1.0060%
48	Zr-95	In-115m	Mixed	20	5	1.0820%	1.0740%
49	Nb-95	In-115m	Mixed	20	5	1.0820%	1.0740%
50	In-115m	Nd-147	Mixed	32	4	1.0820%	1.0742%
51	Zr-95	Cd-115	Mixed	20	5	1.0660%	1.0970%
52	Nb-95	Cd-115	Mixed	20	5	1.0660%	1.0970%
53	Cd-115	Nd-147	Mixed	32	4	1.0660%	1.0971%
54	Nd-147	Pm-151	Both Refractory	4	10	2.0820%	2.0875%
55	Ag-111	Ag-112	Both Volatile	1	5	2.1600%	2.1520%
56	Ag-111	Pd-112	Both Volatile	1	5	2.1590%	2.1750%
57	As-77	Nd-147	Mixed	70	5	2.2870%	2.2680%
58	Ag-112	Nd-147	Mixed	35	6	2.7310%	2.8063%
59	Pd-112	Nd-147	Mixed	35	6	2.7540%	2.8450%
60	Ag-112	Pd-112	Both Volatile	0	5	4.0980%	4.1742%
61	Ag-111	Nd-147	Mixed	36	5	4.9180%	4.9700%
62	Zr-95	Pm-151	Both Refractory	56	8	8.0900%	8.0220%
63	Nb-95	Pm-151	Both Refractory	56	8	9.9750%	9.9550%
64	Zr-95	Nd-147	Both Refractory	52	6	11.2700%	11.3200%
65	Nb-95	Nd-147	Both Refractory	52	8	12.0000%	12.1200%
66	Zr-95	Nb-95	Both Refractory	0	6	26.2500%	26.3000%

Figures 4.5 and 4.6 graphically depict the first zero-error classification pair from Table 4.3 (As-77 and Ag-112), respectively showing the decision tree and activities with decision tree rules outlined. Figure 4.7 shows the decision tree for the pairing of the two radionuclides with the largest mean activities, Nd-147 and Zr-95, and the third largest test error of 11.32%. Figure 4.8 shows Nd-147 vs. Zr-95 activities with the decision node dividers graphically depicted. The poorest performing combination of two radionuclides (Zr-95 and Nb-95) is displayed in Figure

4.9, resulting in 26.3% test misclassification error. The misclassification rate is high because Zr-95 and Nb-95 are in the same mass chain, making them dependent and correlated.

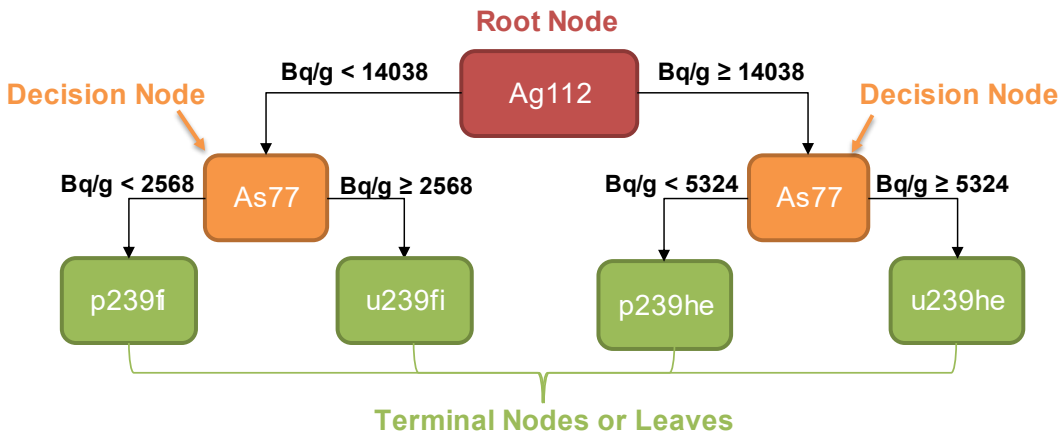

Figure 4.5 Decision tree showing the root node, two decision nodes, and four terminal or leaf nodes using activity levels of Ag-112 and As-77 to classify explosive type.

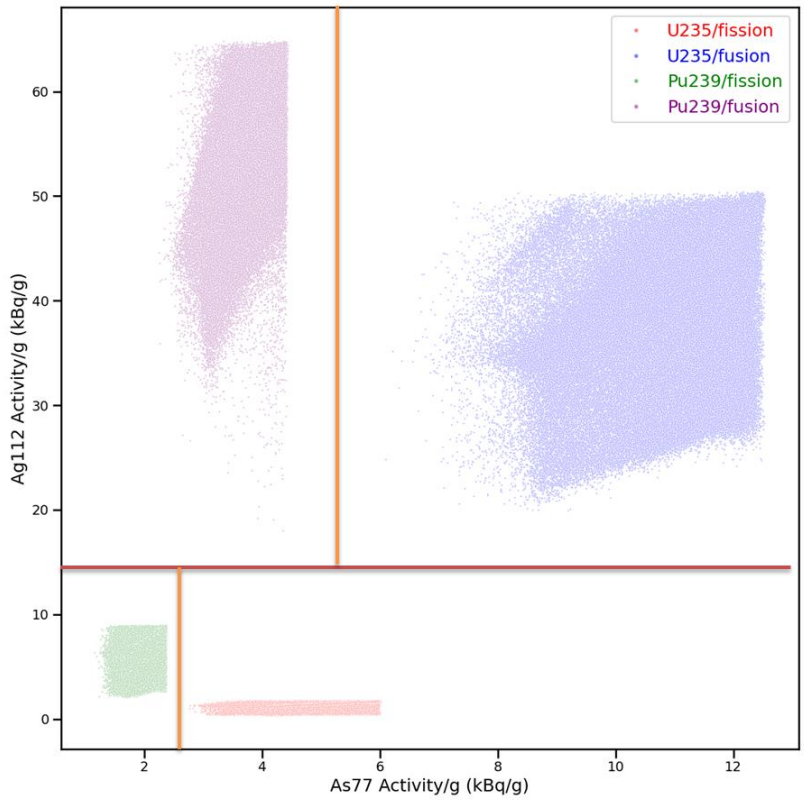

Figure 4.6 Ag-112 vs. As-77 with root (red) and decision node dividers (orange) displayed.

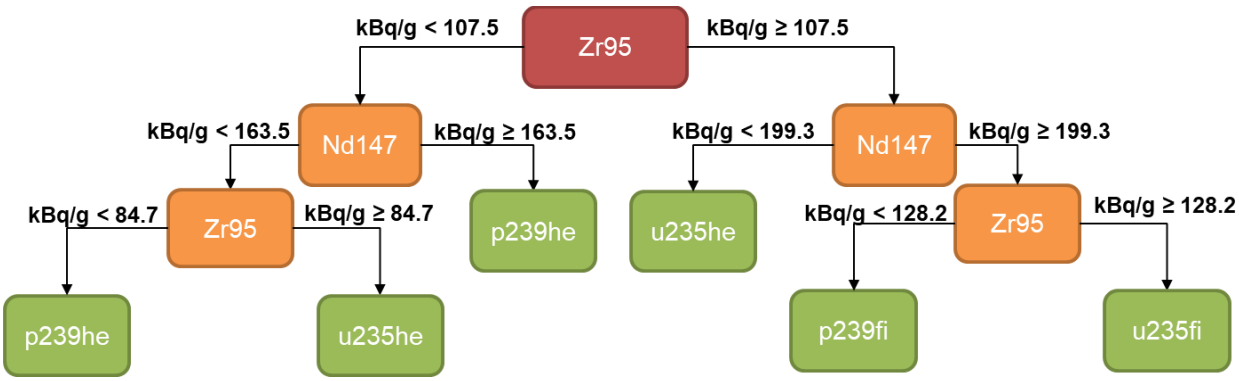

Figure 4.7 Decision tree diagram for radionuclide pair Zr-95 and Nd-147.

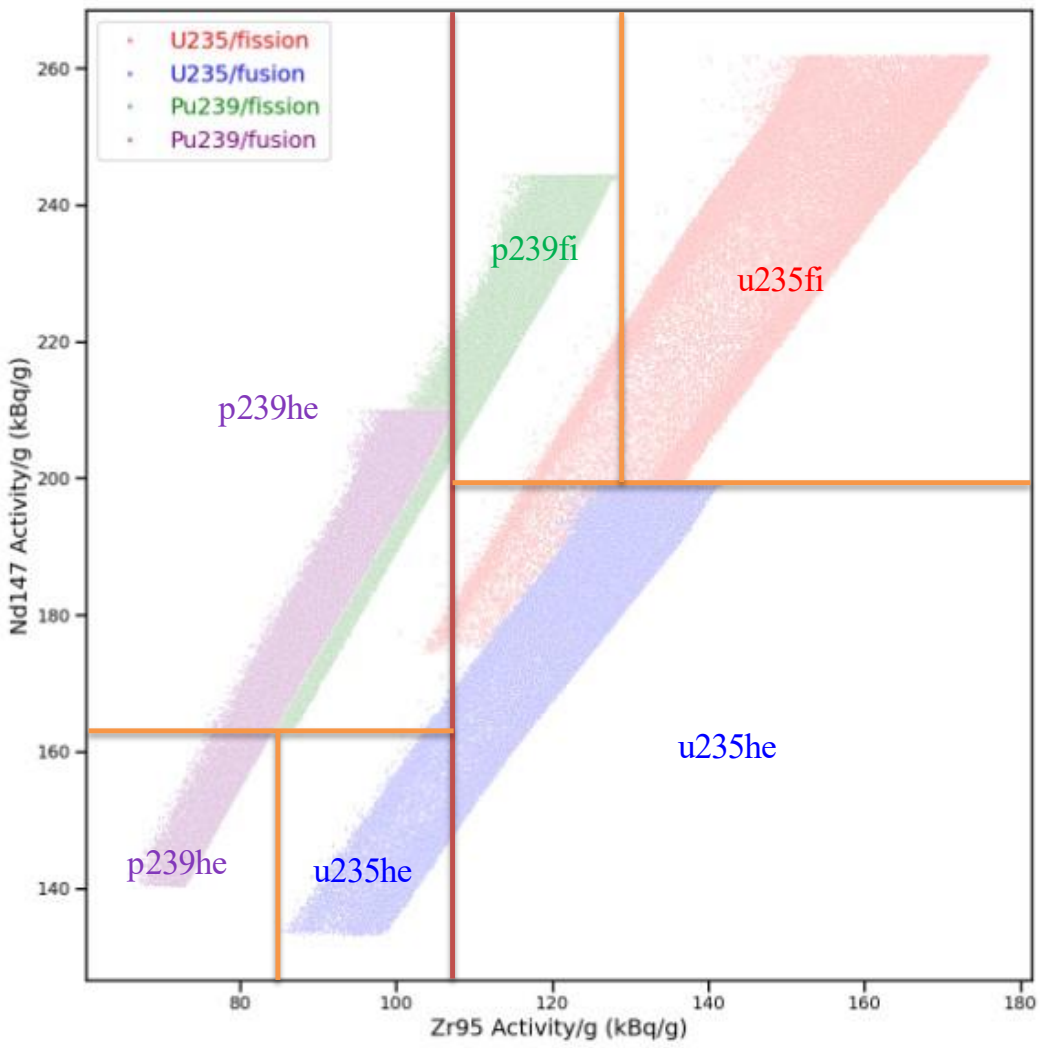

Figure 4.8 Pairwise plot of Nd-147 vs. Zr-95 with root (red) and decision node dividers (orange) displayed.

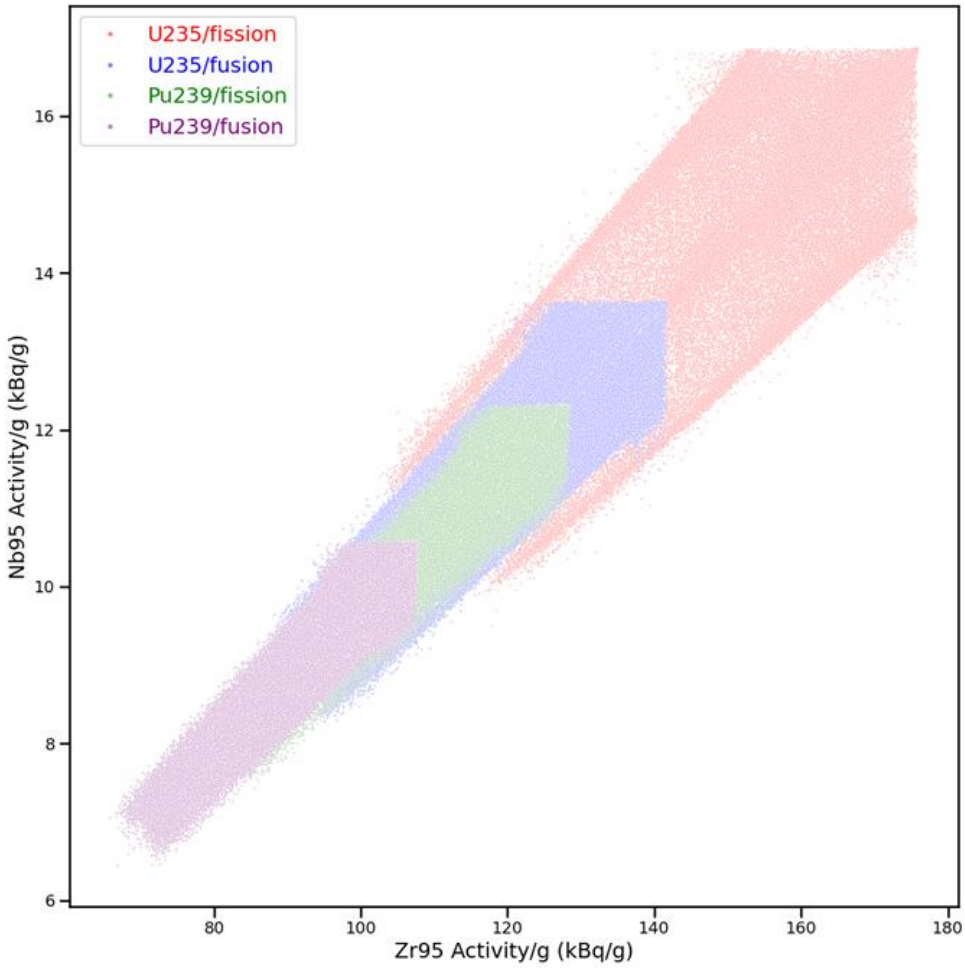

Figure 4.9 Pairwise plot of the activity of Nb-95 vs. Zr-95

The limitations of simple decision trees are apparent in Figure 4.8, where binary recursive partitioning will only cut horizontal and vertical lines to split the data. A model that could approximate diagonal line divisions in the plot would reduce misclassification error for this dataset, although such a model would be less interpretable than the tree diagram with 6 terminal nodes displayed in Figure 4.7.

Figure 4.10 further illustrates this limitation with Zr-95 and Eu-156 paired together. While they result in a low test error of 0.0071%, a model that incorporated diagonal divisions or just a few more subdivisions could classify this pairing with zero error. It will be shown that

random forest classification accomplishes zero error for this and eight other pairings that decision trees could not perfectly classify. However, the attraction of simple decision trees lies in a clearly communicated model versus the ‘black box’ models offered by more complex algorithms.

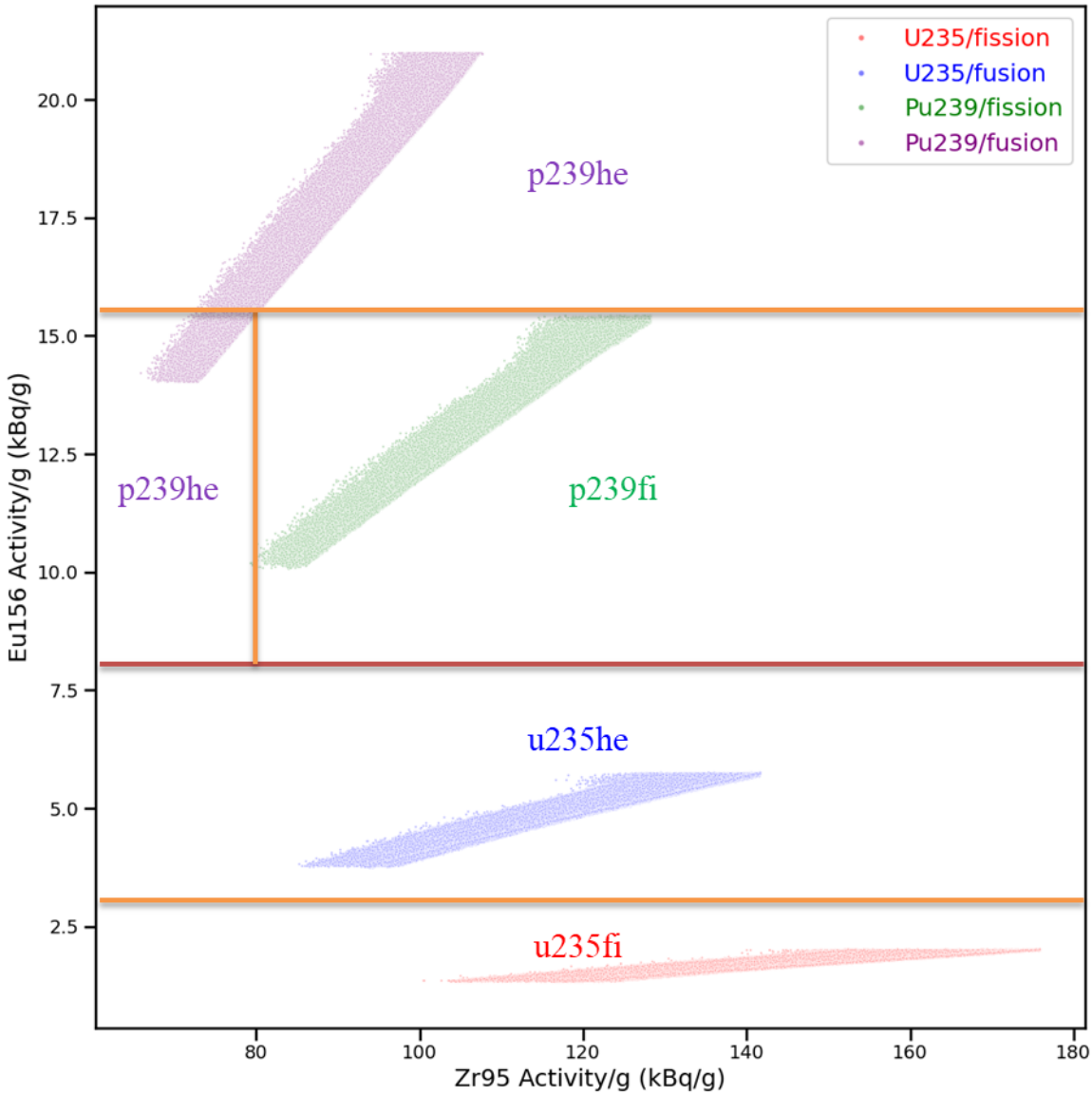

Figure 4.10 Pairwise plot of Eu-156 vs. Zr-95 with root (red) and decision node dividers (orange) displayed.

4.4 Decision Tree Classification for Groups of Three Radionuclides

Combinations of three radionuclides were analyzed using the same decision tree classifiers as the previous two sections. The analysis resulted in 112 of 220 combinations that classify the test data with zero error. In each zero-error case, two of the three radionuclides were zero-error pairings from the previous section. In each case, the decision tree selected the first pair that produced zero error for tree construction and ignored the third radionuclide. Of the remaining combinations, only 11 presented a misclassification error over 1%, with the highest error being 10.92% (Zr-95, Nb-95, and Nd-147). In other words, 209 of 220 three-way combinations can classify explosive type with less than 1% error using simple decision trees. Tables 4.5, 4.6, 4.7, and 4.8 present all combinations.

The poorest classifier combination of three radionuclides (Zr-95, Nb-95, Nd-147) consists of purely refractory fission products. The decision tree for this combination is given in Figure 4.11 with the three-dimensional plot given in Figure 4.12. Recall that Nd-147 was the poorest performing single radionuclide classifier, and that Zr-95 and Nb-95 are a correlated combination from the same mass chain, which all contributed to the higher misclassification rate.

Table 4.5 Groups of three radionuclide combinations ordered by min test error rate (1-55).

Combination	Fission Product 1	Fission Product 2	Fission Product 3	Fractionation Category	Terminal Nodes	Training Misclassification Error Rate (of 560k)	Test Misclassification Error Rate (of 240k)
1	As-77	Zr-95	Ag-112	Mixed	4	0.0000%	0.0000%
2	As-77	Zr-95	Pd-112	Mixed	4	0.0000%	0.0000%
3	As-77	Zr-95	Cd-115	Mixed	4	0.0000%	0.0000%
4	As-77	Zr-95	In-115m	Mixed	4	0.0000%	0.0000%
5	As-77	Nb-95	Ag-112	Mixed	4	0.0000%	0.0000%
6	As-77	Nb-95	Pd-112	Mixed	4	0.0000%	0.0000%
7	As-77	Nb-95	Cd-115	Mixed	4	0.0000%	0.0000%
8	As-77	Nb-95	In-115m	Mixed	4	0.0000%	0.0000%
9	As-77	Ag-111	Ag-112	All Volatile	4	0.0000%	0.0000%
10	As-77	Ag-111	Pd-112	All Volatile	4	0.0000%	0.0000%
11	As-77	Ag-111	Cd-115	All Volatile	4	0.0000%	0.0000%
12	As-77	Ag-111	In-115m	All Volatile	4	0.0000%	0.0000%
13	As-77	Ag-112	Pd-112	All Volatile	4	0.0000%	0.0000%
14	As-77	Ag-112	Cd-115	All Volatile	4	0.0000%	0.0000%
15	As-77	Ag-112	In-115m	All Volatile	4	0.0000%	0.0000%
16	As-77	Ag-112	Nd-147	Mixed	4	0.0000%	0.0000%
17	As-77	Ag-112	Pm-151	Mixed	4	0.0000%	0.0000%
18	As-77	Ag-112	Sm-153	Mixed	4	0.0000%	0.0000%
19	As-77	Ag-112	Eu-156	Mixed	4	0.0000%	0.0000%
20	As-77	Pd-112	Cd-115	All Volatile	4	0.0000%	0.0000%
21	As-77	Pd-112	In-115m	All Volatile	4	0.0000%	0.0000%
22	As-77	Pd-112	Nd-147	Mixed	4	0.0000%	0.0000%
23	As-77	Pd-112	Pm-151	Mixed	4	0.0000%	0.0000%
24	As-77	Pd-112	Sm-153	Mixed	4	0.0000%	0.0000%
25	As-77	Pd-112	Eu-156	Mixed	4	0.0000%	0.0000%
26	As-77	Cd-115	In-115m	All Volatile	4	0.0000%	0.0000%
27	As-77	Cd-115	Nd-147	Mixed	4	0.0000%	0.0000%
28	As-77	Cd-115	Pm-151	Mixed	4	0.0000%	0.0000%
29	As-77	Cd-115	Sm-153	Mixed	4	0.0000%	0.0000%
30	As-77	Cd-115	Eu-156	Mixed	4	0.0000%	0.0000%
31	As-77	In-115m	Nd-147	Mixed	4	0.0000%	0.0000%
32	As-77	In-115m	Pm-151	Mixed	4	0.0000%	0.0000%
33	As-77	In-115m	Sm-153	Mixed	4	0.0000%	0.0000%
34	As-77	In-115m	Eu-156	Mixed	4	0.0000%	0.0000%
35	Zr-95	Ag-112	Pm-151	Mixed	4	0.0000%	0.0000%
36	Zr-95	Ag-112	Sm-153	Mixed	4	0.0000%	0.0000%
37	Zr-95	Ag-112	Eu-156	Mixed	4	0.0000%	0.0000%
38	Zr-95	Pd-112	Pm-151	Mixed	4	0.0000%	0.0000%
39	Zr-95	Pd-112	Sm-153	Mixed	4	0.0000%	0.0000%
40	Zr-95	Pd-112	Eu-156	Mixed	4	0.0000%	0.0000%
41	Zr-95	Cd-115	Pm-151	Mixed	4	0.0000%	0.0000%
42	Zr-95	Cd-115	Sm-153	Mixed	4	0.0000%	0.0000%
43	Zr-95	Cd-115	Eu-156	Mixed	4	0.0000%	0.0000%
44	Zr-95	In-115m	Pm-151	Mixed	4	0.0000%	0.0000%
45	Zr-95	In-115m	Sm-153	Mixed	4	0.0000%	0.0000%
46	Zr-95	In-115m	Eu-156	Mixed	4	0.0000%	0.0000%
47	Nb-95	Ag-112	Pm-151	Mixed	4	0.0000%	0.0000%
48	Nb-95	Ag-112	Sm-153	Mixed	4	0.0000%	0.0000%
49	Nb-95	Ag-112	Eu-156	Mixed	4	0.0000%	0.0000%
50	Nb-95	Pd-112	Pm-151	Mixed	4	0.0000%	0.0000%
51	Nb-95	Pd-112	Sm-153	Mixed	4	0.0000%	0.0000%
52	Nb-95	Pd-112	Eu-156	Mixed	4	0.0000%	0.0000%
53	Nb-95	Cd-115	Pm-151	Mixed	4	0.0000%	0.0000%
54	Nb-95	Cd-115	Sm-153	Mixed	4	0.0000%	0.0000%
55	Nb-95	Cd-115	Eu-156	Mixed	4	0.0000%	0.0000%

Table 4.6 Groups of three radionuclide combinations ordered by min test error rate (56-110).

Combination	Fission Product 1	Fission Product 2	Fission Product 3	Fractionation Category	Terminal Nodes	Training Misclassification Error Rate (of 560k)	Test Misclassification Error Rate (of 240k)
56	Nb-95	In-115m	Pm-151	Mixed	4	0.0000%	0.0000%
57	Nb-95	In-115m	Sm-153	Mixed	4	0.0000%	0.0000%
58	Nb-95	In-115m	Eu-156	Mixed	4	0.0000%	0.0000%
59	Ag-111	Ag-112	Pm-151	Mixed	4	0.0000%	0.0000%
60	Ag-111	Ag-112	Sm-153	Mixed	4	0.0000%	0.0000%
61	Ag-111	Ag-112	Eu-156	Mixed	4	0.0000%	0.0000%
62	Ag-111	Pd-112	Pm-151	Mixed	4	0.0000%	0.0000%
63	Ag-111	Pd-112	Sm-153	Mixed	4	0.0000%	0.0000%
64	Ag-111	Pd-112	Eu-156	Mixed	4	0.0000%	0.0000%
65	Ag-111	Cd-115	Pm-151	Mixed	4	0.0000%	0.0000%
66	Ag-111	Cd-115	Sm-153	Mixed	4	0.0000%	0.0000%
67	Ag-111	Cd-115	Eu-156	Mixed	4	0.0000%	0.0000%
68	Ag-111	In-115m	Pm-151	Mixed	4	0.0000%	0.0000%
69	Ag-111	In-115m	Sm-153	Mixed	4	0.0000%	0.0000%
70	Ag-111	In-115m	Eu-156	Mixed	4	0.0000%	0.0000%
71	Ag-112	Pd-112	Pm-151	Mixed	4	0.0000%	0.0000%
72	Ag-112	Pd-112	Sm-153	Mixed	4	0.0000%	0.0000%
73	Ag-112	Pd-112	Eu-156	Mixed	4	0.0000%	0.0000%
74	Ag-112	Cd-115	Pm-151	Mixed	4	0.0000%	0.0000%
75	Ag-112	Cd-115	Sm-153	Mixed	4	0.0000%	0.0000%
76	Ag-112	Cd-115	Eu-156	Mixed	4	0.0000%	0.0000%
77	Ag-112	In-115m	Pm-151	Mixed	4	0.0000%	0.0000%
78	Ag-112	In-115m	Sm-153	Mixed	4	0.0000%	0.0000%
79	Ag-112	In-115m	Eu-156	Mixed	4	0.0000%	0.0000%
80	Ag-112	Nd-147	Pm-151	Mixed	4	0.0000%	0.0000%
81	Ag-112	Nd-147	Sm-153	Mixed	4	0.0000%	0.0000%
82	Ag-112	Nd-147	Eu-156	Mixed	4	0.0000%	0.0000%
83	Ag-112	Pm-151	Sm-153	Mixed	4	0.0000%	0.0000%
84	Ag-112	Pm-151	Eu-156	Mixed	4	0.0000%	0.0000%
85	Ag-112	Sm-153	Eu-156	Mixed	4	0.0000%	0.0000%
86	Pd-112	Cd-115	Pm-151	Mixed	4	0.0000%	0.0000%
87	Pd-112	Cd-115	Sm-153	Mixed	4	0.0000%	0.0000%
88	Pd-112	Cd-115	Eu-156	Mixed	4	0.0000%	0.0000%
89	Pd-112	In-115m	Pm-151	Mixed	4	0.0000%	0.0000%
90	Pd-112	In-115m	Sm-153	Mixed	4	0.0000%	0.0000%
91	Pd-112	In-115m	Eu-156	Mixed	4	0.0000%	0.0000%
92	Pd-112	Nd-147	Pm-151	Mixed	4	0.0000%	0.0000%
93	Pd-112	Nd-147	Sm-153	Mixed	4	0.0000%	0.0000%
94	Pd-112	Nd-147	Eu-156	Mixed	4	0.0000%	0.0000%
95	Pd-112	Pm-151	Sm-153	Mixed	4	0.0000%	0.0000%
96	Pd-112	Pm-151	Eu-156	Mixed	4	0.0000%	0.0000%
97	Pd-112	Sm-153	Eu-156	Mixed	4	0.0000%	0.0000%
98	Cd-115	In-115m	Pm-151	Mixed	4	0.0000%	0.0000%
99	Cd-115	In-115m	Sm-153	Mixed	4	0.0000%	0.0000%
100	Cd-115	In-115m	Eu-156	Mixed	4	0.0000%	0.0000%
101	Cd-115	Nd-147	Pm-151	Mixed	4	0.0000%	0.0000%
102	Cd-115	Nd-147	Sm-153	Mixed	4	0.0000%	0.0000%
103	Cd-115	Nd-147	Eu-156	Mixed	4	0.0000%	0.0000%
104	Cd-115	Pm-151	Sm-153	Mixed	4	0.0000%	0.0000%
105	Cd-115	Pm-151	Eu-156	Mixed	4	0.0000%	0.0000%
106	Cd-115	Sm-153	Eu-156	Mixed	4	0.0000%	0.0000%
107	In-115m	Nd-147	Pm-151	Mixed	4	0.0000%	0.0000%
108	In-115m	Nd-147	Sm-153	Mixed	4	0.0000%	0.0000%
109	In-115m	Nd-147	Eu-156	Mixed	4	0.0000%	0.0000%
110	In-115m	Pm-151	Sm-153	Mixed	4	0.0000%	0.0000%

Table 4.7 Groups of three radionuclide combinations ordered by min test error rate (110-165).

Combination	Fission Product 1	Fission Product 2	Fission Product 3	Fractionation Category	Terminal Nodes	Training Misclassification Error Rate (of 560k)	Test Misclassification Error Rate (of 240k)
111	In-115m	Pm-151	Eu-156	Mixed	4	0.0000%	0.0000%
112	In-115m	Sm-153	Eu-156	Mixed	4	0.0000%	0.0000%
113	Zr-95	Ag-111	Pm-151	Mixed	4	0.0000%	0.0004%
114	Zr-95	Ag-111	Sm-153	Mixed	4	0.0000%	0.0004%
115	Zr-95	Ag-111	Eu-156	Mixed	4	0.0000%	0.0004%
116	Nb-95	Ag-111	Pm-151	Mixed	4	0.0000%	0.0004%
117	Nb-95	Ag-111	Sm-153	Mixed	4	0.0000%	0.0004%
118	Nb-95	Ag-111	Eu-156	Mixed	4	0.0000%	0.0004%
119	Ag-111	Nd-147	Pm-151	Mixed	4	0.0000%	0.0004%
120	Ag-111	Nd-147	Sm-153	Mixed	4	0.0000%	0.0004%
121	Ag-111	Nd-147	Eu-156	Mixed	4	0.0000%	0.0004%
122	Ag-111	Pm-151	Sm-153	Mixed	4	0.0000%	0.0004%
123	Ag-111	Pm-151	Eu-156	Mixed	4	0.0000%	0.0004%
124	Ag-111	Sm-153	Eu-156	Mixed	4	0.0000%	0.0004%
125	As-77	Ag-111	Pm-151	Mixed	4	0.0000%	0.0008%
126	As-77	Ag-111	Sm-153	Mixed	4	0.0000%	0.0008%
127	As-77	Ag-111	Eu-156	Mixed	4	0.0000%	0.0008%
128	As-77	Zr-95	Pm-151	Mixed	4	0.0018%	0.0021%
129	As-77	Zr-95	Sm-153	Mixed	4	0.0018%	0.0021%
130	As-77	Zr-95	Eu-156	Mixed	4	0.0018%	0.0021%
131	As-77	Nb-95	Pm-151	Mixed	4	0.0018%	0.0021%
132	As-77	Nb-95	Sm-153	Mixed	4	0.0018%	0.0021%
133	As-77	Nb-95	Eu-156	Mixed	4	0.0018%	0.0021%
134	As-77	Nd-147	Pm-151	Mixed	4	0.0018%	0.0021%
135	As-77	Nd-147	Sm-153	Mixed	4	0.0018%	0.0021%
136	As-77	Nd-147	Eu-156	Mixed	4	0.0018%	0.0021%
137	As-77	Pm-151	Sm-153	Mixed	4	0.0018%	0.0021%
138	As-77	Pm-151	Eu-156	Mixed	4	0.0018%	0.0021%
139	As-77	Sm-153	Eu-156	Mixed	4	0.0018%	0.0021%
140	Nb-95	Nd-147	Sm-153	All Refractory	8	0.0018%	0.0038%
141	Nd-147	Pm-151	Sm-153	All Refractory	8	0.0018%	0.0038%
142	Zr-95	Nd-147	Eu-156	All Refractory	5	0.0043%	0.0050%
143	Nb-95	Nd-147	Eu-156	All Refractory	5	0.0043%	0.0050%
144	Nd-147	Pm-151	Eu-156	All Refractory	5	0.0043%	0.0050%
145	Nd-147	Sm-153	Eu-156	All Refractory	5	0.0043%	0.0050%
146	As-77	Zr-95	Ag-111	Mixed	5	0.0039%	0.0058%
147	As-77	Nb-95	Ag-111	Mixed	5	0.0039%	0.0058%
148	As-77	Ag-111	Nd-147	Mixed	5	0.0039%	0.0058%
149	Zr-95	Nb-95	Eu-156	All Refractory	5	0.0045%	0.0071%
150	Zr-95	Pm-151	Eu-156	All Refractory	5	0.0045%	0.0071%
151	Zr-95	Sm-153	Eu-156	All Refractory	5	0.0045%	0.0071%
152	Nb-95	Sm-153	Eu-156	All Refractory	5	0.0095%	0.0104%
153	Nb-95	Pm-151	Eu-156	All Refractory	5	0.0095%	0.0104%
154	Ag-111	Cd-115	In-115m	All Volatile	5	0.0370%	0.0454%
155	Ag-112	Cd-115	In-115m	All Volatile	5	0.0370%	0.0454%
156	Pd-112	Cd-115	In-115m	All Volatile	5	0.0370%	0.0454%
157	As-77	Zr-95	Nb-95	Mixed	5	0.0559%	0.0517%
158	As-77	Zr-95	Nd-147	Mixed	5	0.0559%	0.0517%
159	As-77	Nb-95	Nd-147	Mixed	5	0.1139%	0.1133%
160	Nb-95	Pd-112	Nd-147	Mixed	6	0.1457%	0.1475%
161	Nb-95	Ag-111	Pd-112	Mixed	6	0.1330%	0.1567%
162	Zr-95	Cd-115	In-115m	Mixed	5	0.1746%	0.1779%
163	Nb-95	Cd-115	In-115m	Mixed	5	0.1746%	0.1779%
164	Cd-115	In-115m	Nd-147	Mixed	5	0.1746%	0.1779%
165	Zr-95	Nd-147	Sm-153	All Refractory	8	0.1827%	0.1871%

Table 4.8 Groups of three radionuclide combinations ordered by min test error rate (166-220).

Combination	Fission Product 1	Fission Product 2	Fission Product 3	Fractionation Category	Terminal Nodes	Training Misclassification Error Rate (of 560k)	Test Misclassification Error Rate (of 240k)
166	Zr-95	Ag-111	Cd-115	Mixed	5	0.1914%	0.1920%
167	Nb-95	Ag-111	Cd-115	Mixed	5	0.1914%	0.1920%
168	Ag-111	Ag-112	Cd-115	All Volatile	5	0.1914%	0.1920%
169	Ag-111	Pd-112	Cd-115	All Volatile	5	0.1914%	0.1920%
170	Ag-111	Cd-115	Nd-147	Mixed	5	0.1914%	0.1920%
171	Zr-95	Ag-111	In-115m	Mixed	5	0.1911%	0.2016%
172	Nb-95	Ag-111	In-115m	Mixed	5	0.1911%	0.2016%
173	Ag-111	Ag-112	In-115m	All Volatile	5	0.1911%	0.2016%
174	Ag-111	Pd-112	In-115m	All Volatile	5	0.1911%	0.2016%
175	Ag-111	In-115m	Nd-147	Mixed	5	0.1911%	0.2016%
176	Zr-95	Ag-112	In-115m	Mixed	5	0.2491%	0.2604%
177	Nb-95	Ag-112	In-115m	Mixed	5	0.2491%	0.2604%
178	Ag-112	Pd-112	In-115m	All Volatile	5	0.2491%	0.2604%
179	Ag-112	In-115m	Nd-147	Mixed	5	0.2491%	0.2604%
180	Zr-95	Pd-112	In-115m	Mixed	5	0.2505%	0.2625%
181	Nb-95	Pd-112	In-115m	Mixed	5	0.2505%	0.2625%
182	Pd-112	In-115m	Nd-147	Mixed	5	0.2505%	0.2625%
183	Zr-95	Ag-112	Cd-115	Mixed	5	0.2534%	0.2738%
184	Nb-95	Ag-112	Cd-115	Mixed	5	0.2534%	0.2738%
185	Ag-112	Pd-112	Cd-115	All Volatile	5	0.2534%	0.2738%
186	Ag-112	Cd-115	Nd-147	Mixed	5	0.2534%	0.2738%
187	Zr-95	Pd-112	Cd-115	Mixed	5	0.2593%	0.2792%
188	Nb-95	Pd-112	Cd-115	Mixed	5	0.2593%	0.2792%
189	Pd-112	Cd-115	Nd-147	Mixed	5	0.2593%	0.2792%
190	Zr-95	In-115m	Nd-147	Mixed	6	0.3291%	0.3296%
191	Nb-95	Pm-151	Sm-153	All Refractory	9	0.3211%	0.3337%
192	Zr-95	Cd-115	Nd-147	Mixed	6	0.3321%	0.3417%
193	Nb-95	In-115m	Nd-147	Mixed	6	0.3525%	0.3612%
194	Nb-95	Cd-115	Nd-147	Mixed	6	0.3573%	0.3750%
195	Pm-151	Sm-153	Eu-156	All Refractory	5	0.3668%	0.3875%
196	Zr-95	Nb-95	Ag-112	Mixed	5	0.4975%	0.4975%
197	Zr-95	Ag-111	Ag-112	Mixed	5	0.4975%	0.4975%
198	Zr-95	Ag-112	Pd-112	Mixed	5	0.4975%	0.4975%
199	Zr-95	Ag-112	Nd-147	Mixed	5	0.4975%	0.4975%
200	Zr-95	Nb-95	Pd-112	Mixed	5	0.4793%	0.5079%
201	Zr-95	Ag-111	Pd-112	Mixed	5	0.4793%	0.5079%
202	Zr-95	Pd-112	Nd-147	Mixed	5	0.4793%	0.5079%
203	Zr-95	Nb-95	Sm-153	All Refractory	8	0.5454%	0.5541%
204	Zr-95	Pm-151	Sm-153	All Refractory	8	0.5454%	0.5542%
205	Nb-95	Ag-112	Pd-112	Mixed	5	0.6254%	0.6420%
206	Nb-95	Ag-112	Nd-147	Mixed	5	0.6254%	0.6420%
207	Nb-95	Ag-111	Ag-112	Mixed	5	0.6254%	0.6421%
208	Zr-95	Nb-95	Ag-111	Mixed	5	0.9161%	0.9458%
209	Zr-95	Ag-111	Nd-147	Mixed	5	0.9161%	0.9458%
210	Nb-95	Ag-111	Nd-147	Mixed	5	0.9743%	1.0060%
211	Ag-112	Pd-112	Nd-147	Mixed	7	1.0040%	1.0225%
212	Zr-95	Nb-95	In-115m	Mixed	5	1.0820%	1.0742%
213	Zr-95	Nb-95	Cd-115	Mixed	5	1.0660%	1.0970%
214	Zr-95	Nd-147	Pm-151	All Refractory	10	1.8060%	1.7875%
215	Nb-95	Nd-147	Pm-151	All Refractory	10	2.0820%	2.0875%
216	Ag-111	Ag-112	Nd-147	Mixed	5	2.1600%	2.1520%
217	Ag-111	Ag-112	Pd-112	All Volatile	5	2.1590%	2.1750%
218	Ag-111	Pd-112	Nd-147	Mixed	5	2.1590%	2.1750%
219	Zr-95	Nb-95	Pm-151	All Refractory	11	5.3410%	5.3100%
220	Zr-95	Nb-95	Nd-147	All Refractory	7	10.9200%	10.9913%

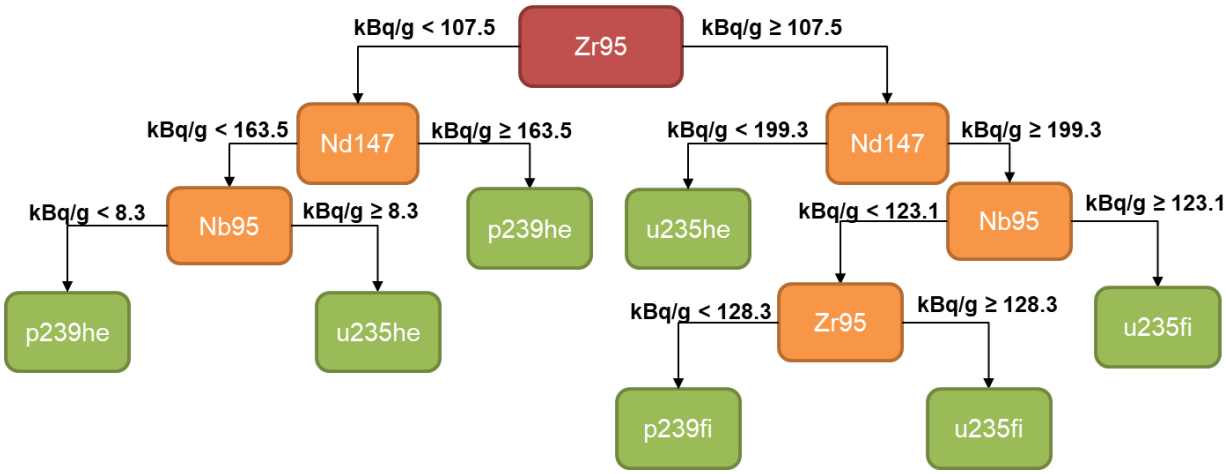

Figure 4.11 Decision tree diagram for radionuclide combination of Zr-95, Nb-95, and Nd-147

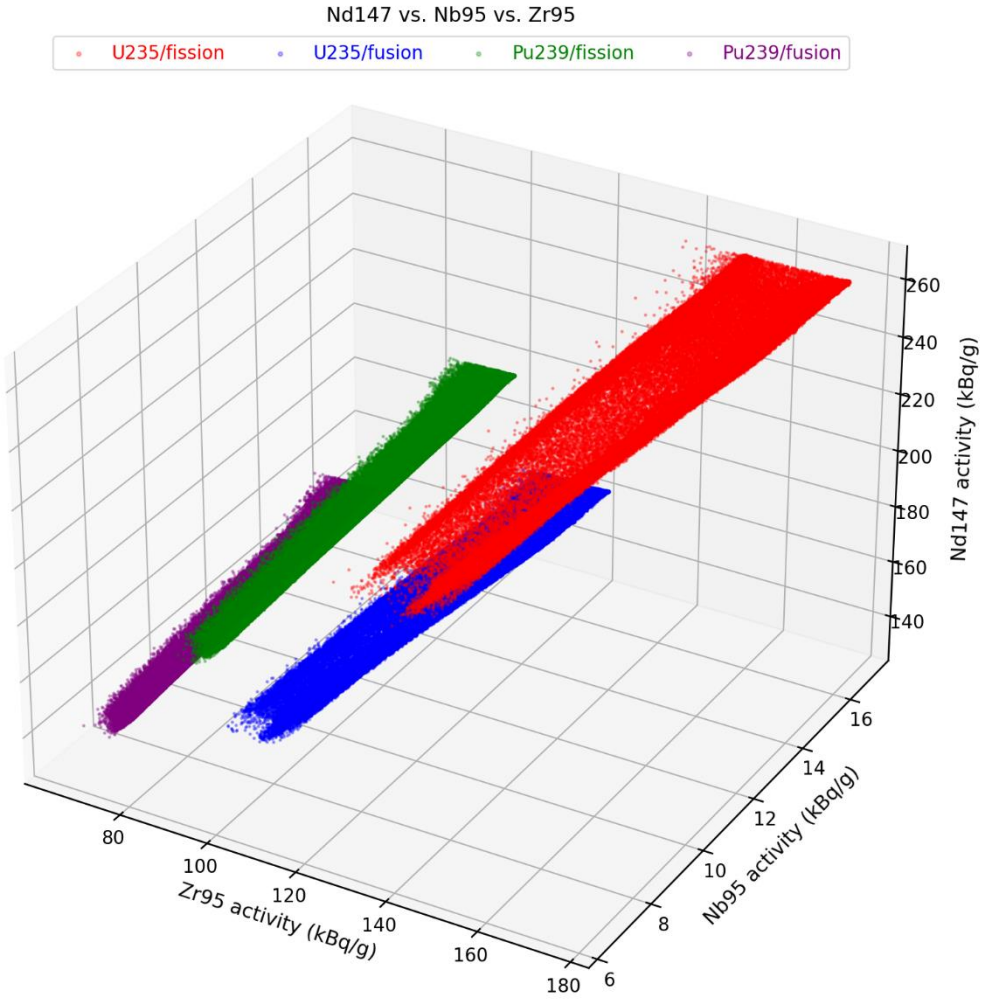

Figure 4.12 Three-dimensional combination plot of Zr-95, Nd-95, and Nd-147.

Figure 4.13 shows a 3D plot of the zero-error combination of As-77, Ag-112, Eu-156. The decision tree for this combination is identical to Figure 3.9 which excludes Eu-156, as As-77 and Ag-112 alone classify the dataset with zero error. When Eu-156 was listed as a feature in the code before As-77, the algorithm constructed a decision tree with Ag-112 and Eu-156, excluding As-77 this time. The algorithm did not continue beyond the first zero-error classifiers it encountered. This remained true as more features were added. When all 12 radionuclides were considered together the resulting simple decision tree always consisted of only the first zero-error pairing the algorithm encountered of pairings 1-16 in Table 4.3.

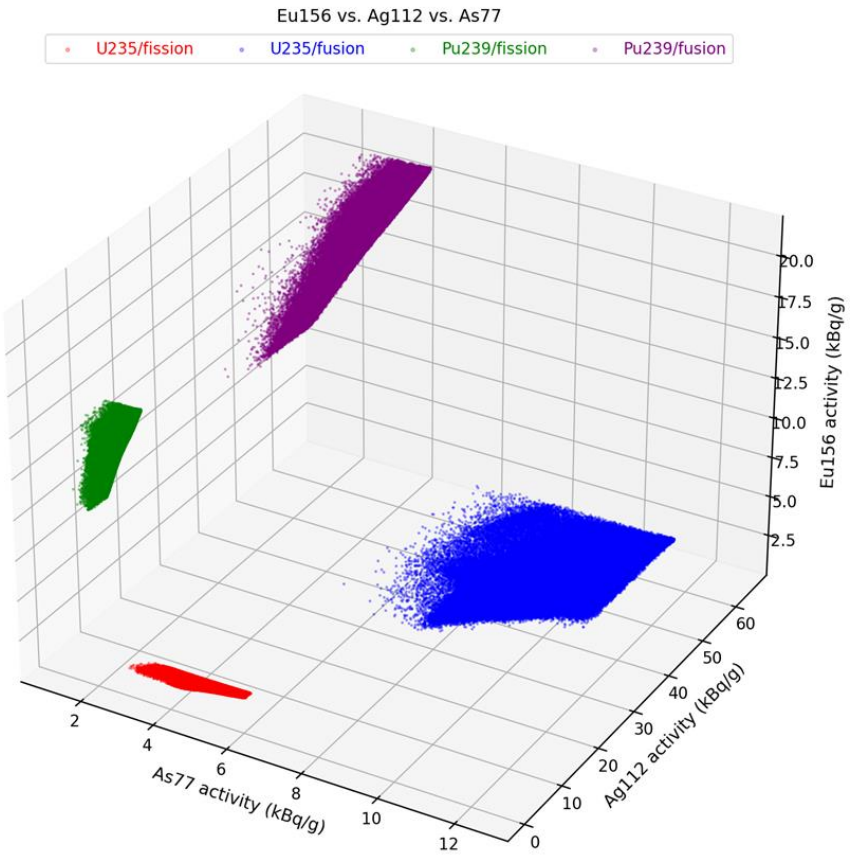

Figure 4.13 Three-dimensional combination plot of As-77, Ag-112, and Eu-156.

4.5 Decision Tree Classification with Four or More Dimensions

Decision tree classification was not conducted for every possible combination of four or more radionuclides, but specific combinations of interest were selected and analyzed. The pairings that produced zero error using simple decision trees are summarized in Table 4.9. When any fission product from Group A was paired with any from Group B, the result was zero misclassifications out of 240,000 tests. Any of these pairings, when included in larger groupings produced a two-radionuclide zero error decision tree. Combinations that exclusive of these pairings all produced some error.

Combining four features, there are 495 possible combinations and 356 of those contain zero error pairings. Of the remaining 139 combinations, the maximum misclassification error was produced by Ag-111, Ag-112, Pd-112, and Nd-147 which was just over 2%, and once again included a radionuclide pair from the same mass chain.

Table 4.9 Listing of fission products for zero-error pairings, when any radionuclide from Group A is combined with any radionuclide from Group B.

Group A	Group B
Ag-112	As-77
Pd-112	Pm-151
Cd-115	Sm-153
In-115m	Eu-156

As more features were added, maximum error rates decreased, until at combinations of 8 there were only two possible combinations that produced error. These are listed in Table 4.10. For all possible combinations of 9-12 fission products, zero error pairings were inevitable, and

each resulting decision tree was two fission products, four terminal nodes, and zero test classification error.

Table 4.10 Combinations of 8 fission products that produce decision tree error.

Combinations of Eight Fission Products Producing Error	**Misclassification Test Error**
Zr-95, Nb-95, Ag-111, Ag-112, Pd-112, Cd-115, In-115m, Nd-147	0.0454%
As-77, Zr-95, Nb-95, Ag-111, Nd-147, Pm-151, Sm-153, Eu-156	0.0008%

Using another approach, all 12 radionuclides were taken together, then the root node radionuclide was eliminated from the model before running it again. These results are given in Table 4.11, showing how the algorithm selected the lowest error combinations it first encountered, and ignored other features that did not further reduce error. The radionuclides are listed in order of elimination.

Table 4.11 Decision tree runs beginning with all 12 radionuclides, where the root node radionuclide designated by "R" is eliminated in each subsequent run.

Run	Pd 112	Ag 112	Cd 115	In 115 m	Pm 151	Sm 153	Eu 156	Ag 111	As 77	Zr 95	Nb 95	Nd 147	Terminal Nodes	Training Misclass of 240,000	Misclass Error Rate
1	R								x				4	0	0%
2		R							x				4	0	0%
3			R						x				4	0	0%
4				R					x				4	0	0%
5					R			x	x				4	2	0.0008%
6						R		x	x				4	2	0.0008%
7							R	x	x				4	2	0.0008%
8								R	x				5	14	0.0058%
9									R	x			5	124	0.0517%
10										R	x	x	7	26,379	10.99%
11											R	x	8	29,081	12.12%
12												R	5	99,402	41.32%

4.6 Random Forest Classification

Random forest models cannot improve on a model that exhibits zero error, so they were only used to examine combinations of fission products that produced error in decision tree classification. The random forest technique is intended for larger feature sets since the algorithm uses random feature selection to reduce bagging correlation. For this reason, only combinations of two or more fission products were considered. A forest of 500 trees was used. The number of features selected at each split was optimized to minimize test error. The training set for random forests was reduced to 175,000 realizations (about 1/3 of the decision tree training set) due to the computational demand of the more complex model.

For combinations of two fission products, random forest classification was able to classify 25 of the 66 combinations with zero error, finding 9 more zero-error pairings than simple

decision trees. Table 4.12 shows the new random forest zero-error pairings additional to the 16 found in Table 4.9 by decision trees. There were 50 radionuclide pairs from decision tree classification that produced non-zero classification error, and random forest classification reduced error in 41 of those same combinations. The error reductions ranged from minimal (0.01%) to substantial (8.54%). There were 6 combinations where random forest produced marginally higher error (< 0.5% total increase). Tables 4.13 and 4.14 list radionuclide pairs and error data for random forest classification.

Plots for many of these pairings are previously shown in this thesis. Notably, Figure 3.13 shows Sm-153 vs. Zr-95, which is a new zero-error pairing with random forest. Figure 4.7 shows Eu-156 vs. Zr-95, another new random forest classification pairing with zero error.

Table 4.12 Zero-test error pairings possible with random forest classification in addition to the 16 pairings from Table 4.9.

New Zero Error Pairings Using Random Forest		
Sm-153 vs. Zr-95	Sm-153 vs. Pm-151	Eu-156 vs. Nd-147
Sm-153 vs. Nb-95	Eu-156 vs. Zr-95	Eu-156 vs. Pm-151
Sm-153 vs. Nd-147	Eu-156 vs. Nb-95	Eu-156 vs. Sm-153

Table 4.13 Groups of two radionuclide combinations ordered by largest to smallest total test error change between decision trees and random forest (1-33).

Combination	Fission Product 1	Fission Product 2	Decision Tree Error Rate	Random Forest Error Rate	Total Error Change
1	Nb-95	Pm-151	9.9550%	1.4171%	-8.5379%
2	Zr-95	Nd-147	11.3200%	3.1058%	-8.2142%
3	Zr-95	Pm-151	8.0220%	1.3029%	-6.7191%
4	Zr-95	Nb-95	26.3000%	21.7925%	-4.5075%
5	Nb-95	Nd-147	12.1200%	8.1896%	-3.9304%
6	Ag-111	Nd-147	4.9700%	2.2158%	-2.7542%
7	Nd-147	Pm-151	2.0875%	0.0017%	-2.0858%
8	As-77	Nd-147	2.2680%	0.2308%	-2.0372%
9	Pd-112	Nd-147	2.8450%	1.0467%	-1.7983%
10	Ag-112	Nd-147	2.8063%	1.0108%	-1.7955%
11	Zr-95	Cd-115	1.0970%	0.3271%	-0.7699%
12	Nb-95	Cd-115	1.0970%	0.3550%	-0.7420%
13	Zr-95	In-115m	1.0740%	0.3513%	-0.7227%
14	Nb-95	In-115m	1.0740%	0.3733%	-0.7007%
15	Nb-95	Ag-111	1.0060%	0.3071%	-0.6989%
16	Nb-95	Ag-112	0.6420%	0.0563%	-0.5857%
17	Zr-95	Sm-153	0.5541%	0.0000%	-0.5541%
18	Zr-95	Ag-111	0.7958%	0.2754%	-0.5204%
19	In-115m	Nd-147	1.0742%	0.6108%	-0.4634%
20	Zr-95	Pd-112	0.5079%	0.0488%	-0.4591%
21	Cd-115	Nd-147	1.0971%	0.6404%	-0.4567%
22	Zr-95	Ag-112	0.4975%	0.0525%	-0.4450%
23	Pm-151	Eu-156	0.3875%	0.0000%	-0.3875%
24	Nb-95	Sm-153	0.3337%	0.0000%	-0.3337%
25	Ag-111	Ag-112	2.1520%	1.9942%	-0.1578%
26	Cd-115	In-115m	0.1779%	0.0442%	-0.1337%
27	Ag-111	Pd-112	2.1750%	2.0642%	-0.1108%
28	Nb-95	Pd-112	0.1475%	0.0558%	-0.0917%
29	As-77	Nb-95	0.1550%	0.1079%	-0.0471%
30	Pm-151	Sm-153	0.0400%	0.0000%	-0.0400%
31	Ag-111	Pm-151	0.0171%	0.0004%	-0.0167%
32	Ag-111	Sm-153	0.0171%	0.0008%	-0.0163%
33	Ag-111	Eu-156	0.0171%	0.0008%	-0.0163%

Table 4.14 Groups of two radionuclide combinations ordered by largest to smallest total test error change between decision trees and random forest (34-66).

Combination	Fission Product 1	Fission Product 2	Decision Tree Error Rate	Random Forest Error Rate	Total Error Change
34	As-77	Zr-95	0.0517%	0.0388%	-0.0129%
35	Nb-95	Eu-156	0.0104%	0.0000%	-0.0104%
36	Zr-95	Eu-156	0.0071%	0.0000%	-0.0071%
37	Nd-147	Eu-156	0.0050%	0.0000%	-0.0050%
38	Sm-153	Eu-156	0.0050%	0.0000%	-0.0050%
39	As-77	Ag-111	0.0058%	0.0017%	-0.0041%
40	Nd-147	Sm-153	0.0038%	0.0000%	-0.0038%
41	Pd-112	Cd-115	0.2792%	0.2771%	-0.0021%
42	As-77	Ag-112	0.0000%	0.0000%	0.0000%
43	As-77	Pd-112	0.0000%	0.0000%	0.0000%
44	As-77	Cd-115	0.0000%	0.0000%	0.0000%
45	As-77	In-115m	0.0000%	0.0000%	0.0000%
46	Ag-112	Pm-151	0.0000%	0.0000%	0.0000%
47	Ag-112	Sm-153	0.0000%	0.0000%	0.0000%
48	Ag-112	Eu-156	0.0000%	0.0000%	0.0000%
49	Pd-112	Pm-151	0.0000%	0.0000%	0.0000%
50	Pd-112	Sm-153	0.0000%	0.0000%	0.0000%
51	Pd-112	Eu-156	0.0000%	0.0000%	0.0000%
52	Cd-115	Pm-151	0.0000%	0.0000%	0.0000%
53	Cd-115	Sm-153	0.0000%	0.0000%	0.0000%
54	Cd-115	Eu-156	0.0000%	0.0000%	0.0000%
55	In-115m	Pm-151	0.0000%	0.0000%	0.0000%
56	In-115m	Sm-153	0.0000%	0.0000%	0.0000%
57	In-115m	Eu-156	0.0000%	0.0000%	0.0000%
58	As-77	Pm-151	0.0021%	0.0021%	0.0000%
59	As-77	Sm-153	0.0021%	0.0021%	0.0000%
60	As-77	Eu-156	0.0021%	0.0021%	0.0000%
61	Ag-112	Cd-115	0.2738%	0.2767%	0.0029%
62	Ag-111	In-115m	0.2016%	0.2092%	0.0076%
63	Ag-111	Cd-115	0.1920%	0.2000%	0.0080%
64	Ag-112	In-115m	0.2604%	0.2713%	0.0109%
65	Pd-112	In-115m	0.2625%	0.2738%	0.0113%
66	Ag-112	Pd-112	4.1742%	4.6333%	0.4591%

The poorest classifying combinations of three were Zr-95, Nb-95, and Nd-147 (all refractory with two belonging to the same mass chain). For decision tree classification, they produced a test error of just under 11% (Table 4.8). With random forest classification the test error rate was 1.89%.

The combination of three fission products that had a high minimum activity across all explosive types and a large test error was Zr-95, Nd-147, and Pm-151 (all refractory). They produced a decision tree test error of about 1.8%. With random forest classification, there was zero test error.

Random forest classification was able to classify 165 out of the 220 possible combinations of three with zero error on a reduced training set of about 175,000 realizations, identifying 43 more zero-error combinations than decision tree classification. Only two of the combinations presented a classification error rate greater than 0.3%. A summary of combinations of three is listed in Tables 4.15 and 4.16, comparing random forest results to decision tree results. They are listed in the same order as Tables 4.5-4.8 to enable comparison.

Table 4.15 Groups of three radionuclide combinations ordered by min tree test error rate with random forest (RF) test error rate and change in error from tree to random forest (1-110).

Combo	Fission Product 1	Fission Product 2	Fission Product 3	TreeTest Error Rate	RF Test Error Rate	Change In Error
1	As-77	Zr-95	Ag-112	0.0000%	0.0000%	0.0000%
2	As-77	Zr-95	Pd-112	0.0000%	0.0000%	0.0000%
3	As-77	Zr-95	Cd-115	0.0000%	0.0000%	0.0000%
4	As-77	Zr-95	In-115m	0.0000%	0.0000%	0.0000%
5	As-77	Nb-95	Ag-112	0.0000%	0.0000%	0.0000%
6	As-77	Nb-95	Pd-112	0.0000%	0.0000%	0.0000%
7	As-77	Nb-95	Cd-115	0.0000%	0.0000%	0.0000%
8	As-77	Nb-95	In-115m	0.0000%	0.0000%	0.0000%
9	As-77	Ag-111	Ag-112	0.0000%	0.0000%	0.0000%
10	As-77	Ag-111	Pd-112	0.0000%	0.0000%	0.0000%
11	As-77	Ag-111	Cd-115	0.0000%	0.0000%	0.0000%
12	As-77	Ag-111	In-115m	0.0000%	0.0000%	0.0000%
13	As-77	Ag-112	Pd-112	0.0000%	0.0000%	0.0000%
14	As-77	Ag-112	Cd-115	0.0000%	0.0000%	0.0000%
15	As-77	Ag-112	In-115m	0.0000%	0.0000%	0.0000%
16	As-77	Ag-112	Nd-147	0.0000%	0.0000%	0.0000%
17	As-77	Ag-112	Pm-151	0.0000%	0.0000%	0.0000%
18	As-77	Ag-112	Sm-153	0.0000%	0.0000%	0.0000%
19	As-77	Ag-112	Eu-156	0.0000%	0.0000%	0.0000%
20	As-77	Pd-112	Cd-115	0.0000%	0.0000%	0.0000%
21	As-77	Pd-112	In-115m	0.0000%	0.0000%	0.0000%
22	As-77	Pd-112	Nd-147	0.0000%	0.0000%	0.0000%
23	As-77	Pd-112	Pm-151	0.0000%	0.0000%	0.0000%
24	As-77	Pd-112	Sm-153	0.0000%	0.0000%	0.0000%
25	As-77	Pd-112	Eu-156	0.0000%	0.0000%	0.0000%
26	As-77	Cd-115	In-115m	0.0000%	0.0000%	0.0000%
27	As-77	Cd-115	Nd-147	0.0000%	0.0000%	0.0000%
28	As-77	Cd-115	Pm-151	0.0000%	0.0000%	0.0000%
29	As-77	Cd-115	Sm-153	0.0000%	0.0000%	0.0000%
30	As-77	Cd-115	Eu-156	0.0000%	0.0000%	0.0000%
31	As-77	In-115m	Nd-147	0.0000%	0.0000%	0.0000%
32	As-77	In-115m	Pm-151	0.0000%	0.0000%	0.0000%
33	As-77	In-115m	Sm-153	0.0000%	0.0000%	0.0000%
34	As-77	In-115m	Eu-156	0.0000%	0.0000%	0.0000%
35	Zr-95	Ag-112	Pm-151	0.0000%	0.0000%	0.0000%
36	Zr-95	Ag-112	Sm-153	0.0000%	0.0000%	0.0000%
37	Zr-95	Ag-112	Eu-156	0.0000%	0.0000%	0.0000%
38	Zr-95	Pd-112	Pm-151	0.0000%	0.0000%	0.0000%
39	Zr-95	Pd-112	Sm-153	0.0000%	0.0000%	0.0000%
40	Zr-95	Pd-112	Eu-156	0.0000%	0.0000%	0.0000%
41	Zr-95	Cd-115	Pm-151	0.0000%	0.0000%	0.0000%
42	Zr-95	Cd-115	Sm-153	0.0000%	0.0000%	0.0000%
43	Zr-95	Cd-115	Eu-156	0.0000%	0.0000%	0.0000%
44	Zr-95	In-115m	Pm-151	0.0000%	0.0000%	0.0000%
45	Zr-95	In-115m	Sm-153	0.0000%	0.0000%	0.0000%
46	Zr-95	In-115m	Eu-156	0.0000%	0.0000%	0.0000%
47	Nb-95	Ag-112	Pm-151	0.0000%	0.0000%	0.0000%
48	Nb-95	Ag-112	Sm-153	0.0000%	0.0000%	0.0000%
49	Nb-95	Ag-112	Eu-156	0.0000%	0.0000%	0.0000%
50	Nb-95	Pd-112	Pm-151	0.0000%	0.0000%	0.0000%
51	Nb-95	Pd-112	Sm-153	0.0000%	0.0000%	0.0000%
52	Nb-95	Pd-112	Eu-156	0.0000%	0.0000%	0.0000%
53	Nb-95	Cd-115	Pm-151	0.0000%	0.0000%	0.0000%
54	Nb-95	Cd-115	Sm-153	0.0000%	0.0000%	0.0000%
55	Nb-95	Cd-115	Eu-156	0.0000%	0.0000%	0.0000%
56	Nb-95	In-115m	Pm-151	0.0000%	0.0000%	0.0000%
57	Nb-95	In-115m	Sm-153	0.0000%	0.0000%	0.0000%
58	Nb-95	In-115m	Eu-156	0.0000%	0.0000%	0.0000%
59	Ag-111	Ag-112	Pm-151	0.0000%	0.0000%	0.0000%
60	Ag-111	Ag-112	Sm-153	0.0000%	0.0000%	0.0000%
61	Ag-111	Ag-112	Eu-156	0.0000%	0.0000%	0.0000%
62	Ag-111	Pd-112	Pm-151	0.0000%	0.0000%	0.0000%
63	Ag-111	Pd-112	Sm-153	0.0000%	0.0000%	0.0000%
64	Ag-111	Pd-112	Eu-156	0.0000%	0.0000%	0.0000%
65	Ag-111	Cd-115	Pm-151	0.0000%	0.0000%	0.0000%
66	Ag-111	Cd-115	Sm-153	0.0000%	0.0000%	0.0000%
67	Ag-111	Cd-115	Eu-156	0.0000%	0.0000%	0.0000%
68	Ag-111	In-115m	Pm-151	0.0000%	0.0000%	0.0000%
69	Ag-111	In-115m	Sm-153	0.0000%	0.0000%	0.0000%
70	Ag-111	In-115m	Eu-156	0.0000%	0.0000%	0.0000%
71	Ag-112	Pd-112	Pm-151	0.0000%	0.0000%	0.0000%
72	Ag-112	Pd-112	Sm-153	0.0000%	0.0000%	0.0000%
73	Ag-112	Pd-112	Eu-156	0.0000%	0.0000%	0.0000%
74	Ag-112	Cd-115	Pm-151	0.0000%	0.0000%	0.0000%
75	Ag-112	Cd-115	Sm-153	0.0000%	0.0000%	0.0000%
76	Ag-112	Cd-115	Eu-156	0.0000%	0.0000%	0.0000%
77	Ag-112	In-115m	Pm-151	0.0000%	0.0000%	0.0000%
78	Ag-112	In-115m	Sm-153	0.0000%	0.0000%	0.0000%
79	Ag-112	In-115m	Eu-156	0.0000%	0.0000%	0.0000%
80	Ag-112	Nd-147	Pm-151	0.0000%	0.0000%	0.0000%
81	Ag-112	Nd-147	Sm-153	0.0000%	0.0000%	0.0000%
82	Ag-112	Nd-147	Eu-156	0.0000%	0.0000%	0.0000%
83	Ag-112	Pm-151	Sm-153	0.0000%	0.0000%	0.0000%
84	Ag-112	Pm-151	Eu-156	0.0000%	0.0000%	0.0000%
85	Ag-112	Sm-153	Eu-156	0.0000%	0.0000%	0.0000%
86	Pd-112	Cd-115	Pm-151	0.0000%	0.0000%	0.0000%
87	Pd-112	Cd-115	Sm-153	0.0000%	0.0000%	0.0000%
88	Pd-112	Cd-115	Eu-156	0.0000%	0.0000%	0.0000%
89	Pd-112	In-115m	Pm-151	0.0000%	0.0000%	0.0000%
90	Pd-112	In-115m	Sm-153	0.0000%	0.0000%	0.0000%
91	Pd-112	In-115m	Eu-156	0.0000%	0.0000%	0.0000%
92	Pd-112	Nd-147	Pm-151	0.0000%	0.0000%	0.0000%
93	Pd-112	Nd-147	Sm-153	0.0000%	0.0000%	0.0000%
94	Pd-112	Nd-147	Eu-156	0.0000%	0.0000%	0.0000%
95	Pd-112	Pm-151	Sm-153	0.0000%	0.0000%	0.0000%
96	Pd-112	Pm-151	Eu-156	0.0000%	0.0000%	0.0000%
97	Pd-112	Sm-153	Eu-156	0.0000%	0.0000%	0.0000%
98	Cd-115	In-115m	Pm-151	0.0000%	0.0000%	0.0000%
99	Cd-115	In-115m	Sm-153	0.0000%	0.0000%	0.0000%
100	Cd-115	In-115m	Eu-156	0.0000%	0.0000%	0.0000%
101	Cd-115	Nd-147	Pm-151	0.0000%	0.0000%	0.0000%
102	Cd-115	Nd-147	Sm-153	0.0000%	0.0000%	0.0000%
103	Cd-115	Nd-147	Eu-156	0.0000%	0.0000%	0.0000%
104	Cd-115	Pm-151	Sm-153	0.0000%	0.0000%	0.0000%
105	Cd-115	Pm-151	Eu-156	0.0000%	0.0000%	0.0000%
106	Cd-115	Sm-153	Eu-156	0.0000%	0.0000%	0.0000%
107	In-115m	Nd-147	Pm-151	0.0000%	0.0000%	0.0000%
108	In-115m	Nd-147	Sm-153	0.0000%	0.0000%	0.0000%
109	In-115m	Nd-147	Eu-156	0.0000%	0.0000%	0.0000%
110	In-115m	Pm-151	Sm-153	0.0000%	0.0000%	0.0000%

Table 4.16 Groups of three radionuclide combinations ordered by min tree test error rate with random forest (RF) test error rate and change in error from tree to random forest (111-220).

Combo	Fission Product 1	Fission Product 2	Fission Product 3	TreeTest Error Rate	RF Test Error Rate	Change In Error
111	In-115m	Pm-151	Eu-156	0.0000%	0.0000%	0.0000%
112	In-115m	Sm-153	Eu-156	0.0000%	0.0000%	0.0000%
113	Zr-95	Ag-111	Pm-151	0.0004%	0.0000%	-0.0004%
114	Zr-95	Ag-111	Sm-153	0.0004%	0.0000%	-0.0004%
115	Zr-95	Ag-111	Eu-156	0.0004%	0.0000%	-0.0004%
116	Nb-95	Ag-111	Pm-151	0.0004%	0.0000%	-0.0004%
117	Nb-95	Ag-111	Sm-153	0.0004%	0.0000%	-0.0004%
118	Nb-95	Ag-111	Eu-156	0.0004%	0.0000%	-0.0004%
119	Ag-111	Nd-147	Pm-151	0.0004%	0.0000%	-0.0004%
120	Ag-111	Nd-147	Sm-153	0.0004%	0.0000%	-0.0004%
121	Ag-111	Nd-147	Eu-156	0.0004%	0.0000%	-0.0004%
122	Ag-111	Pm-151	Sm-153	0.0004%	0.0000%	-0.0004%
123	Ag-111	Pm-151	Eu-156	0.0004%	0.0000%	-0.0004%
124	Ag-111	Sm-153	Eu-156	0.0004%	0.0000%	-0.0004%
125	As-77	Ag-111	Pm-151	0.0008%	0.0000%	-0.0008%
126	As-77	Ag-111	Sm-153	0.0008%	0.0017%	0.0009%
127	As-77	Ag-111	Eu-156	0.0008%	0.0017%	0.0009%
128	As-77	Zr-95	Pm-151	0.0021%	0.0017%	-0.0004%
129	As-77	Zr-95	Sm-153	0.0021%	0.0000%	-0.0021%
130	As-77	Zr-95	Eu-156	0.0021%	0.0000%	-0.0021%
131	As-77	Nb-95	Pm-151	0.0021%	0.0004%	-0.0017%
132	As-77	Nb-95	Sm-153	0.0021%	0.0000%	-0.0021%
133	As-77	Nb-95	Eu-156	0.0021%	0.0000%	-0.0021%
134	As-77	Nd-147	Pm-151	0.0021%	0.0000%	-0.0021%
135	As-77	Nd-147	Sm-153	0.0021%	0.0000%	-0.0021%
136	As-77	Nd-147	Eu-156	0.0021%	0.0000%	-0.0021%
137	As-77	Pm-151	Sm-153	0.0021%	0.0000%	-0.0021%
138	As-77	Pm-151	Eu-156	0.0021%	0.0000%	-0.0021%
139	As-77	Sm-153	Eu-156	0.0021%	0.0000%	-0.0021%
140	Nb-95	Nd-147	Sm-153	0.0038%	0.0000%	-0.0038%
141	Nd-147	Pm-151	Sm-153	0.0038%	0.0000%	-0.0038%
142	Zr-95	Nd-147	Eu-156	0.0050%	0.0000%	-0.0050%
143	Nb-95	Nd-147	Eu-156	0.0050%	0.0000%	-0.0050%
144	Nd-147	Pm-151	Eu-156	0.0050%	0.0000%	-0.0050%
145	Nd-147	Sm-153	Eu-156	0.0050%	0.0000%	-0.0050%
146	As-77	Zr-95	Ag-111	0.0058%	0.0000%	-0.0058%
147	As-77	Nb-95	Ag-111	0.0058%	0.0004%	-0.0054%
148	As-77	Ag-111	Nd-147	0.0058%	0.0000%	-0.0058%
149	Zr-95	Nb-95	Eu-156	0.0071%	0.0000%	-0.0071%
150	Zr-95	Pm-151	Eu-156	0.0071%	0.0000%	-0.0071%
151	Zr-95	Sm-153	Eu-156	0.0071%	0.0000%	-0.0071%
152	Nb-95	Sm-153	Eu-156	0.0104%	0.0000%	-0.0104%
153	Nb-95	Pm-151	Eu-156	0.0104%	0.0000%	-0.0104%
154	Ag-111	Cd-115	In-115m	0.0454%	0.0100%	-0.0354%
155	Ag-112	Cd-115	In-115m	0.0454%	0.0154%	-0.0300%
156	Pd-112	Cd-115	In-115m	0.0454%	0.0125%	-0.0329%
157	As-77	Zr-95	Nb-95	0.0517%	0.0042%	-0.0475%
158	As-77	Zr-95	Nd-147	0.0517%	0.0000%	-0.0517%
159	As-77	Nb-95	Nd-147	0.1133%	0.0000%	-0.1133%
160	Nb-95	Pd-112	Nd-147	0.1475%	0.0000%	-0.1475%
161	Nb-95	Ag-111	Pd-112	0.1567%	0.0008%	-0.1559%
162	Zr-95	Cd-115	In-115m	0.1779%	0.0108%	-0.1671%
163	Nb-95	Cd-115	In-115m	0.1779%	0.0104%	-0.1675%
164	Cd-115	In-115m	Nd-147	0.1779%	0.0279%	-0.1500%
165	Zr-95	Nd-147	Sm-153	0.1871%	0.0000%	-0.1871%
166	Zr-95	Ag-111	Cd-115	0.1920%	0.0021%	-0.1899%
167	Nb-95	Ag-111	Cd-115	0.1920%	0.0046%	-0.1874%
168	Ag-111	Ag-112	Cd-115	0.1920%	0.0992%	-0.0928%
169	Ag-111	Pd-112	Cd-115	0.1920%	0.0958%	-0.0962%
170	Ag-111	Cd-115	Nd-147	0.1920%	0.0775%	-0.1145%
171	Zr-95	Ag-111	In-115m	0.2016%	0.0038%	-0.1978%
172	Nb-95	Ag-111	In-115m	0.2016%	0.0054%	-0.1962%
173	Ag-111	Ag-112	In-115m	0.2016%	0.0992%	-0.1024%
174	Ag-111	Pd-112	In-115m	0.2016%	0.0975%	-0.1041%
175	Ag-111	In-115m	Nd-147	0.2016%	0.0842%	-0.1174%
176	Zr-95	Ag-112	In-115m	0.2604%	0.0021%	-0.2583%
177	Nb-95	Ag-112	In-115m	0.2604%	0.0021%	-0.2583%
178	Ag-112	Pd-112	In-115m	0.2604%	0.1796%	-0.0808%
179	Ag-112	In-115m	Nd-147	0.2604%	0.0563%	-0.2041%
180	Zr-95	Pd-112	In-115m	0.2625%	0.0038%	-0.2587%
181	Nb-95	Pd-112	In-115m	0.2625%	0.0050%	-0.2575%
182	Pd-112	In-115m	Nd-147	0.2625%	0.0471%	-0.2154%
183	Zr-95	Ag-112	Cd-115	0.2738%	0.0025%	-0.2713%
184	Nb-95	Ag-112	Cd-115	0.2738%	0.0021%	-0.2717%
185	Ag-112	Pd-112	Cd-115	0.2738%	0.1958%	-0.0780%
186	Ag-112	Cd-115	Nd-147	0.2738%	0.0533%	-0.2205%
187	Zr-95	Pd-112	Cd-115	0.2792%	0.0008%	-0.2784%
188	Nb-95	Pd-112	Cd-115	0.2792%	0.0017%	-0.2775%
189	Pd-112	Cd-115	Nd-147	0.2792%	0.0438%	-0.2354%
190	Zr-95	In-115m	Nd-147	0.3296%	0.0000%	-0.3296%
191	Nb-95	Pm-151	Sm-153	0.3337%	0.0000%	-0.3337%
192	Zr-95	Cd-115	Nd-147	0.3417%	0.0008%	-0.3409%
193	Nb-95	In-115m	Nd-147	0.3612%	0.0000%	-0.3612%
194	Nb-95	Cd-115	Nd-147	0.3750%	0.0004%	-0.3746%
195	Pm-151	Sm-153	Eu-156	0.3875%	0.0000%	-0.3875%
196	Zr-95	Nb-95	Ag-112	0.4975%	0.0483%	-0.4492%
197	Zr-95	Ag-111	Ag-112	0.4975%	0.0021%	-0.4954%
198	Zr-95	Ag-112	Pd-112	0.4975%	0.0008%	-0.4967%
199	Zr-95	Ag-112	Nd-147	0.4975%	0.0000%	-0.4975%
200	Zr-95	Nb-95	Pd-112	0.5079%	0.0446%	-0.4633%
201	Zr-95	Ag-111	Pd-112	0.5079%	0.0013%	-0.5066%
202	Zr-95	Pd-112	Nd-147	0.5079%	0.0000%	-0.5079%
203	Zr-95	Nb-95	Sm-153	0.5541%	0.0000%	-0.5541%
204	Zr-95	Pm-151	Sm-153	0.5542%	0.0000%	-0.5542%
205	Nb-95	Ag-112	Pd-112	0.6420%	0.0000%	-0.6420%
206	Nb-95	Ag-112	Nd-147	0.6420%	0.0000%	-0.6420%
207	Nb-95	Ag-111	Ag-112	0.6421%	0.0013%	-0.6408%
208	Zr-95	Nb-95	Ag-111	0.9458%	0.2354%	-0.7104%
209	Zr-95	Ag-111	Nd-147	0.9458%	0.0000%	-0.9458%
210	Nb-95	Ag-111	Nd-147	1.0060%	0.0000%	-1.0060%
211	Ag-112	Pd-112	Nd-147	1.0225%	0.0788%	-0.9437%
212	Zr-95	Nb-95	In-115m	1.0742%	0.2513%	-0.8229%
213	Zr-95	Nb-95	Cd-115	1.0970%	0.2592%	-0.8378%
214	Zr-95	Nd-147	Pm-151	1.7875%	0.0000%	-1.7875%
215	Nb-95	Nd-147	Pm-151	2.0875%	0.0013%	-2.0862%
216	Ag-111	Ag-112	Nd-147	2.1520%	0.1571%	-1.9949%
217	Ag-111	Ag-112	Pd-112	2.1750%	1.3975%	-0.7775%
218	Ag-111	Pd-112	Nd-147	2.1750%	0.1479%	-2.0271%
219	Zr-95	Nb-95	Pm-151	5.3100%	0.1992%	-5.1108%
220	Zr-95	Nb-95	Nd-147	10.9913%	1.8888%	-9.1025%

Random forest classification was not conducted for every possible combination of four or more radionuclides, but specific combinations of interest were analyzed. With combinations of four, the poorest performing random forest models with their respective errors for decision tree and random forest classification are given in Table 4.17. Note the prevalence of mass chain 112 duplicates in these combinations, and the two combinations with the largest random forest error also have mass chains within four nucleons of the others (111 to 115).

Table 4.17 Combinations of 4 fission products producing the highest random forest test errors.

Poorest Classifying Combinations of Four Fission Products	**Decision Tree Test Error**	**Random Forest Test Error**
Ag-111, Ag-112, Pd-112, Nd-147	2.17 %	0.02%
Ag-111, Ag-112, Pd-112, Cd-115	0.20%	0.08%
Ag-111, Ag-112, Pd-112, In-115m	0.20%	0.08%

The four fission products with the highest minimum activity across all explosive types (Zr-95, Nd-147, Pm-151, Sm-153) were analyzed. The decision tree error was about 0.2% and the random forest error was zero.

Specific combinations of five fission products were analyzed. The error rates for random forest classification either drop to zero or become vanishingly small, the largest being less than 0.005% error from Ag-111, Ag-112, Pd-112, Cd-115, and In115m. Note that each of the radionuclides has a mass number within four of every other, with several belonging to the same mass chains.

For combinations of six, there is only a single combination producing any error using random forest classification: Ag-111, Ag-112, Pd-112, Cd-115, In115m, and Nd-147. The test error for this combination is about 0.001%.

Random forest classifiers reduced error in nearly every case for combinations where single decision tree models produced error. Random forest was able to classify many combinations with zero error that decision trees could not. Random forest classification required about 3x more computational time and produced less interpretable models. Within acceptable error levels, simple decision tree models are recommended for this dataset. Random forest classification would be useful for specific combinations where decision tree classification exhibits unacceptable error. This could be the case if, for example, 2 or 3 radionuclides of the 12 were easily observed in sample gamma spectra and were not modeled well with simple decision trees.

4.7 Gradient Boosting Classification

Gradient boosting was conducted on the poorest classifiers of three and four radionuclides. For the combinations analyzed, the computational time required to optimize gradient boosting hyperparameters was greater than random forest run time by more than an order of magnitude and yielded results with no significant improvement over random forest.

For the combination of the three poorest classifiers (Zr-95, Nb-95, and Nd-147), gradient boosting results in a classification error rate of 2%, similar to random forest classification. The relative influence output graph for the fission products is given in Figure 4.14. Gradient boosting is useful for identifying which features have the largest influence on the response when there are many features. For example, if over 100 gammas were determined to be observable in fallout gamma spectra, gradient boosting may be useful in determining their relative value for classification of explosive type in order to down-select the number of features for making an interpretable decision tree model. For the purposes of this analysis however, there were few

enough features that they were analyzed individually and as combinations successfully using interpretable models, making gradient boosting feature selection superfluous.

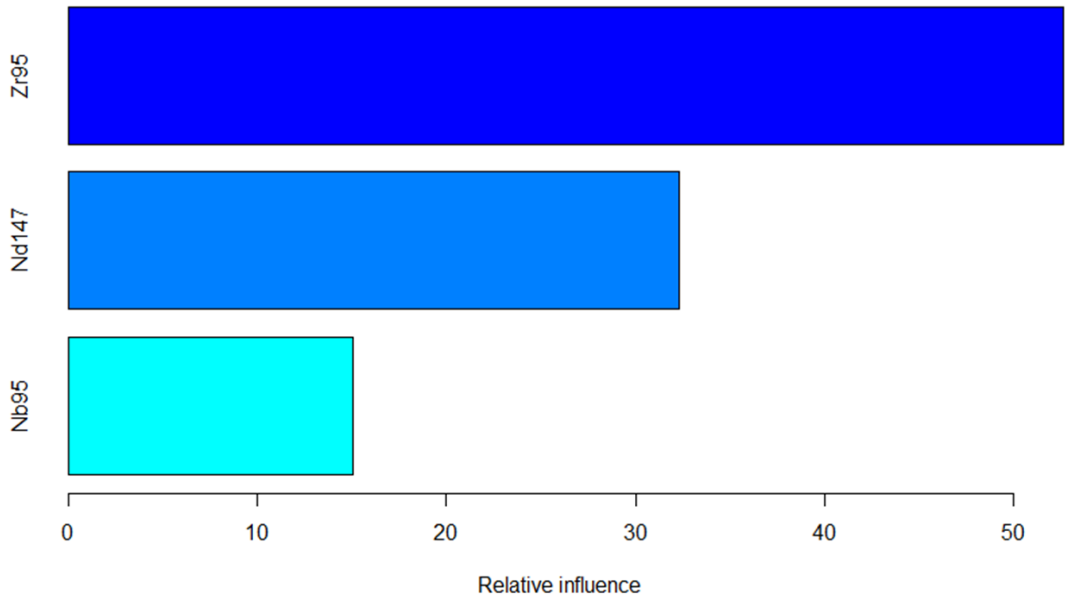

Figure 4.14 Relative influence graph for Zr-95, Nb-95, and Nd-147 tuned gradient boosting model.

For the poorest classifying combination of four radionuclides in random forest (Ag-111, Ag-112, Pd-112, and Cd-115), classification test error using gradient boosting was similarly 0.08%. The relative influence output graph for the fission products if given in Figure 4.15.

The computational time required to tune gradient boosting models to improve upon random forest performance by insignificant margins made gradient boosting modeling an ineffective technique for this dataset. For a dataset with larger error resulting from decision tree and random forest models, gradient boosting could become worthwhile, as may other methods not explored here.

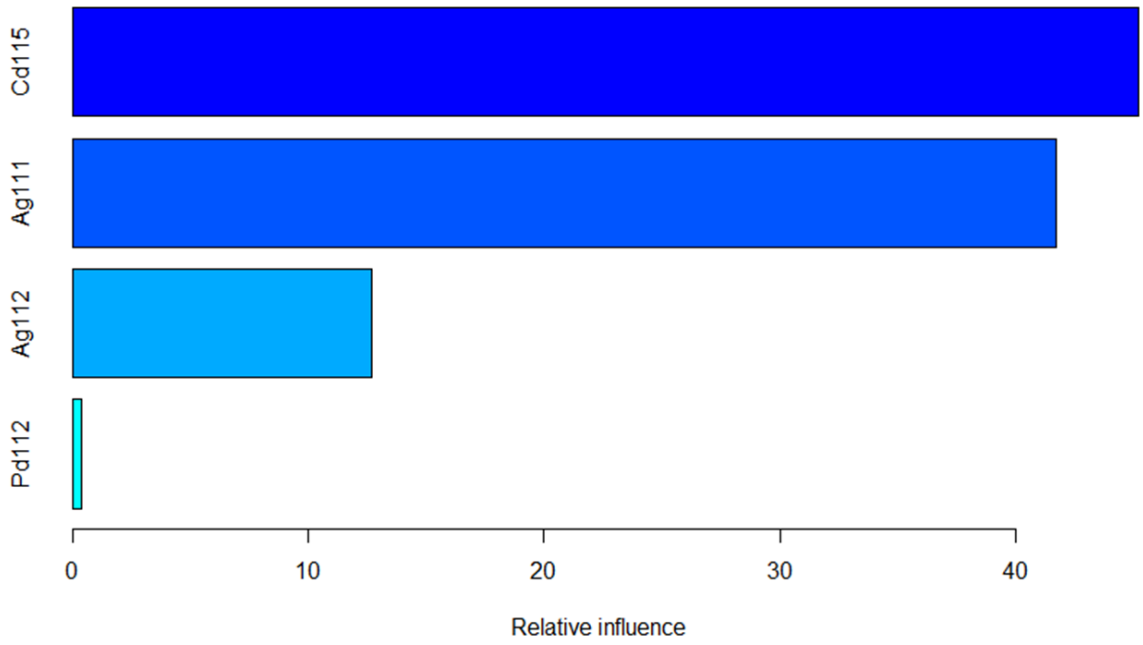

Figure 4.15 Relative influence graph for Ag-111, Ag-112, Pd-112, and Cd-115 tuned gradient boosting model.

4.8 Radionuclide Observability

The observability of radionuclides is critical to their application in gamma spectroscopy. The activity of the 12 radionuclides analyzed here was briefly discussed at the start of this chapter and mean activity levels shown with Figure 4.1. Additional important considerations are the detector efficiency, gamma energy, and the gamma intensity.

Detector efficiency varies across the gamma energy spectrum. Figure 4.16 shows the energy-dependent detector efficiency for the Detective-EX100, a human-portable high-purity germanium (HPGe) detector often used in post-detonation field diagnostics. [43] This detector's intrinsic efficiency only exceeds 40% between 85 and 300 keV, and like most gamma spectroscopic instruments, it has a lower level discriminator at roughly 20-30 keV to exclude electronic noise. Detector efficiency should be factored into radionuclide observability.

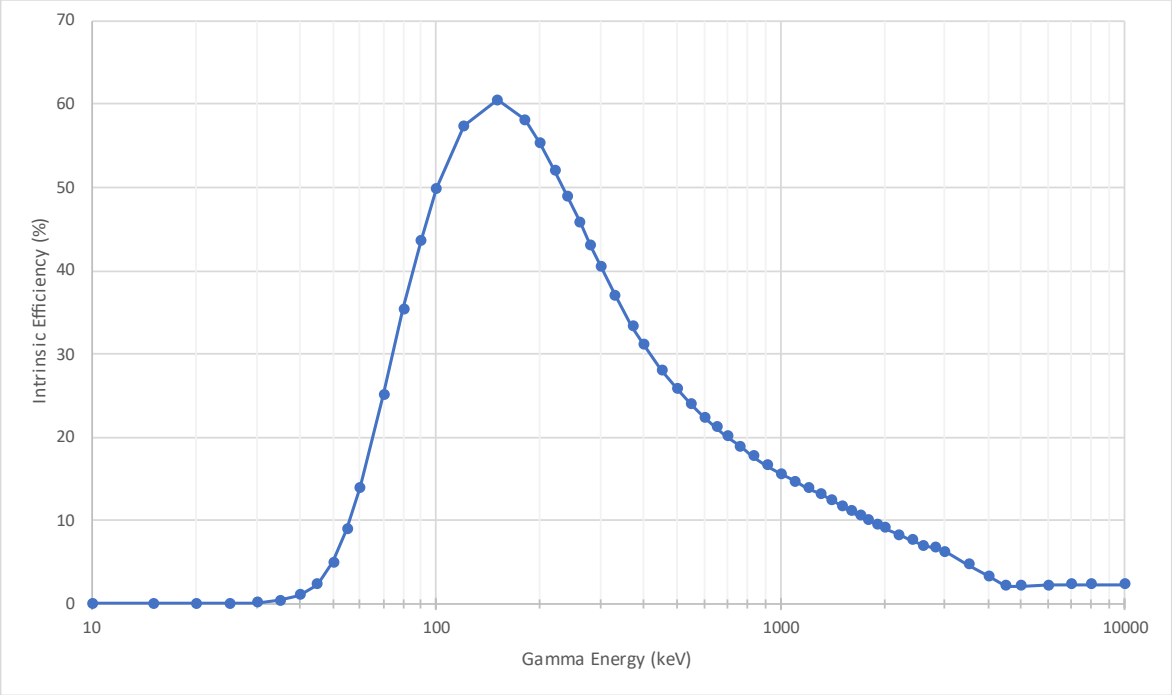

Figure 4.16 Efficiency of the Detective-EX100.

Gamma emission is represented by probabilities. A radionuclide decay has a probability (a.k.a., intensity) of emitting a characteristic gamma photon at a discrete energy. For the 12 given radionuclides, there are 519 total characteristic gammas possible. [44] Table 4.18 gives the number of characteristic gammas for the 12 radionuclides of interest. Of these, there are four gammas that are below 20 keV which can be omitted. Of note, the only characteristic gamma of Pd-112 is 18.5 keV. Therefore, Pd-112 would not be identifiable in the gamma spectra of a sample, reducing the potentially useful list of radionuclides from 12 to 11.

Table 4.18 Number of characteristic gammas per nuclide. Gammas above 20keV are listed in parentheses.

Nuclide	# of Characteristic Gammas (# above 20 keV)	Nuclide	# of Characteristic Gammas (# above 20 keV)
As-77	15 (14)	Cd-115	18 (18)
Zr-95	3 (3)	In-115m	1 (1)
Nb-95	3 (3)	Nc-147	26 (26)
Ag-111	14 (14)	Pm-151	200 (199)
Ag-112	90 (90)	Sm-153	50 (49)
Pd-112	1 (0)	Eu-156	97 (97)

The intensities of the 515 remaining characteristic gammas span from 99.8% (765.8 keV gamma from Nb-95) to 8 x 10^{-6} % (344.2 keV gamma from Cd-115). Using a minimum cutoff of 1% intensity, 71 characteristic gammas remain. Each of the 11 radionuclides exhibit at least one gamma in this reduced list.

Weighted gamma intensity is given in Equation 4.1:

$$I_j^w = \varepsilon_j \times I_j \qquad \textbf{(4.1)}$$

where weighted gamma intensity (I^w) is the product of detector efficiency (ε) and gamma intensity (I) for each gamma (j). Combining this weighted intensity with the parent nuclide activity provides insight into the potential for the gamma to be observed in the spectrum. A short list of the gammas with the largest weighted gamma intensities is provided in Table 4.19. All 26 gammas with a weighted intensity over 1% are listed. Note the many zero-error pairings possible in the list (reference Table 4.9), with Group A gammas highlighted in green, and Group B

gammas highlighted in blue. Of the remaining four radionuclides, three are included in zero error pairings identified in random forest classification (reference Table 4.12).

Table 4.19 Gammas with weighted intensities exceeding 1%.

Symbol	Energy (keV)	Gamma Intensity (%)	Efficiency (%)	Weighted Intensity (%)
Nb95	765.80	99.81	18.81	18.77
Cd115	336.24	46.02	36.45	16.77
In115m	336.24	45.90	36.45	16.73
Sm153	103.18	29.14	51.09	14.89
Nd147	91.11	28.90	44.34	12.81
Zr95	756.73	54.38	18.97	10.31
Ag112	617.52	43.00	22.00	9.46
Zr95	724.19	44.27	19.61	8.68
Pm151	340.08	22.50	36.09	8.12
Cd115	527.90	27.45	24.72	6.79
Pm151	167.75	8.30	59.07	4.90
Eu156	88.97	8.40	42.80	3.59
Nd147	531.01	13.11	24.60	3.23
Pm151	275.21	6.80	43.65	2.97
Ag111	342.13	6.70	35.90	2.41
Pm151	177.16	3.80	58.33	2.22
Cd115	492.35	8.03	26.10	2.10
Pm151	240.09	3.80	48.82	1.86
Pm151	104.84	3.50	51.72	1.81
Eu156	811.77	9.70	18.04	1.75
Eu156	646.29	6.30	21.31	1.34
Pm151	100.02	2.54	49.91	1.27
Sm153	69.67	4.67	24.69	1.15
Pm151	445.68	4.00	28.34	1.13
Eu156	1230.71	8.00	13.67	1.09
Eu156	723.47	5.40	19.63	1.06

A more thorough investigation of gamma observability is outside of the scope of this thesis but would complement it substantially. Specifically, identifying distinguishable gammas from fallout for the radionuclides used in this work would be useful for comparison with the known zero-error classification combinations identified.

Work detailing how fission product activity can be extracted from gamma spectra has been the subject of several dissertations like that of Smith [45]. By using observable gammas from fallout samples to extract fission product activities for radionuclides, the machine learning methods explored in this work could be directly applied to classify weapon type.

4.9 Consolidated Results

- This research identified combinations of fission products that classified explosive type even when predictions of fallout composition incorporated large uncertainties in input thermodynamic coefficients, and with no assumed knowledge of variations in explosive yield and burst height.
- Most combinations of fission products across the machine learning types analyzed could classify explosive type with low or zero error rates. As fission products were added from diverse mass chains, existing error rates were significantly reduced or reached zero. Combinations with fission products from of the same mass chain predictably resulted in poorer performance, as far more can be inferred by combinations of fission products that are not directly correlated.
- Decision tree classification offered low or zero error classification for most combinations. For combinations that produced error decision tree classification was consistently outperformed by random forest classification.
- Decision tree classification provided simple and interpretable models regardless of performance. Random forest and gradient boosting models do not provide interpretable classification models.

- Decision tree overfitting was not observed in this research because the dataset was large (200,000 realizations per explosive type) and the decision tree algorithm had a tree growth depth limit imposed.
- Decision tree instability was not observed in this research, with training set size and seed number alterations producing <5% variation in activity levels for decision nodes and no change in tree structure or selected features.
- Gradient boosting could match but provided no notable improvement over random forest learning. Each gradient boosting run required an order of magnitude time increase for model tuning and training over random forest and was deemed impractical for this dataset.
- Pd-112, one of the 12 radionuclides analyzed in this work, is not practically observable in gamma spectra. The low energy (18.6 keV) of its single characteristic gamma falls below the lower-level discriminator setting of most gamma spectroscopic instruments.
- Limited observability analysis considered the highest weighted intensities (>1%) for the characteristic gammas of the radionuclides of interest. There were 26 characteristic gammas above this threshold, representing 9 of the radionuclides of interest. Most of the zero-error classification combinations identified in this research stem from the 9 identified radionuclides with higher observability.

CHAPTER 5: CONCLUSIONS AND FUTURE WORK

5.1 Conclusions

The goal of this thesis was to use supervised machine learning to classify explosive type from predicted fallout composition data. The data were simulated using surrogate models based on the Korts and Norman fallout formation model implemented in DELFIC. The surrogate models enabled uncertainties in the thermodynamic parameters governing fractionation to be propagated onto the KN model's predictions of fallout composition. Classification tools including decision tree classification, random forest classification, and gradient boosting were applied to the simulated data to identify combinations of fission products that classify explosive type when the thermodynamic parameters were varied ± 50% of their nominal values.

A set of 12 fission product radionuclides were selected for this analysis based on their separation in activity for different explosive types and their high activity per unit fallout mass. Four explosive types were simulated with 200,000 realizations. The data were separated into training and testing sets for use with supervised machine learning classification.

Decision tree classification provided simple and interpretable models that classified explosive type. It was able to identify 16 radionuclide pairs (Table 4.9) that classified explosive type with zero error, and many other groupings that resulted in very low classification error (Tables 4.3 - 4.8 and 4.10). Decision tree classification exhibited maximum errors of 26.3% for combinations of two and 11% for combinations of three fission products.

Random forest classification produced more accurate but less interpretable models. Random forest could not improve on decision tree models that classified explosive type with zero error. They did, however, improve classification for combinations that produced error with decision tree classification. Random forest identified nine additional pairings that could produce

zero error (Table 4.12) and exhibited maximum errors of 4.6% for combinations of two fission products and 1.9% for combinations of three fission products.

The gradient boosting method required significant hyperparameter tuning to optimize models. Several combinations with misclassification error from random forest classification were selected and analyzed using gradient boosting, but gradient boosting yielded no significant improvement on random forest results despite order of magnitude greater computational run times. Given the smaller run times and low misclassification error rates achieved by the first two methods, gradient boosting was not practical for this dataset.

Limited observability analysis considered the highest weighted intensities (>1%) for the characteristic gammas of the radionuclides of interest. There were 26 characteristic gammas above this threshold, representing 9 of the radionuclides of interest. Most of the zero-error classification combinations identified in this research stem from the 9 identified radionuclides with higher observability.

This work showed that there are machine learning methods that can classify explosive type with a high degree of accuracy when trained on computational predictions of fallout composition. These methods could assist in prompt classification of explosive type when combined with in-situ high resolution gamma spectroscopy shortly after a nuclear detonation. They can also be used to identify fission products that would be useful for explosive type classification if their thermodynamic properties were measured more precisely.

5.2 Future Work

There are several classification methods that were not explored in this research but could also prove helpful in classification of fallout composition. Specifically, methods like nearest neighbors, support vector machines, and gaussian processes could prove beneficial.

A more thorough investigation of gamma observability would complement this work. Specifically, identifying distinguishable gammas in fallout gamma spectra would be useful for comparison with the dominant gammas of the radionuclides used here for classification. Those gammas could be used to measure the activity of some fission products and enable direct application of the machine learning classification methods in this research.

REFERENCES

[1] H. G. Norment, DELFIC: Department of Defense Fallout Prediction System: Volume I - Fundamentals, Washington D.C.: Defense Nuclear Agency, 1979.

[2] EUROPEAN POLICE OFFICE, INTERNATIONAL ATOMIC ENERGY AGENCY, INTERNATIONAL POLICE ORGANIZATION, WORLD CUSTOMS ORGANIZATION, "Combating Illicit Trafficking in Nuclear and Other Radioactive Material," in *IAEA Nuclear Security Series No. 6*, Vienna, 2007.

[3] I. Kwai, "Iran Turns Off U.N. Surveillance Cameras at Nuclear Site," *The New York Times*, 8 June 2022.

[4] B. a. H. Albright, "Iran's Natanz Tunnel Complex: Deeper, Larger than Expected," Institute for Science and International Security, Washington D.C., 2022.

[5] L. Thomas-Greenfield, "Security Council Fails to Adopt Resolution Tightening Sanctions Regime in Democratic People's Republic of Korea, as Two Members Wield Veto," in *United Nations: Meetings Coverage and Press Releases*, New York City, 2022.

[6] R. Pszczel, "The Consequences of Russia's Invasion of Ukraine for International Secuirty - NATO and Beyond," *NATO Review*, 7 July 2022.

[7] Office of the Secratary of Defense, "Military and Secuirty Developments Involving the People's Republic of China," in *A Report to Congress Pursuant to the National Defense Authorization Act for Fiscal Year 2000*, Washington D.C., 2021.

[8] "H.R. 2631, The Nuclear Forensics and Attribution Act," in *Hearing before the Subcommittee on Emerging Threats, Cybersecurity, and Science and Technology*, Washington D.C., 2007.

[9] International Atomic Energy Agency, "Nuclear Forensics In Support of Investigations: Implementing Guide," *IAEA Nuclear Security Series*, no. No. 2-G (Rev.1), pp. 19-25, 2015.

[10] W. Cassata, N. Gharibyan, B. Isselhardt, J. Matzel and T. Parsons-Davis, "Nuclear Forensics," Lawrence Livermore National Laboratory, Livermore, 2022.

[11] E. C. Freiling, "Fractionation in Suface Bursts," in *Radioactive Fallout from Nuclear Weapons Tests*, Germantown, 1961.

[12] R. E. Heft, "The Characterization of Radioactive Particles from Nuclear Weapons Tests," *Advances in Chemistry; American Chemical Society*, vol. 7, no. 2, pp. 254-281, 1970.

[13] R. F. Korts and J. H. Norman, "A Calculational Model for Condensed State Diffusion Controlled Fission Product Absorption During Fallout Formation," General Atomic Project 564 for the Office of Civil Defense, Washington D.C., 1967.

[14] C. Parks, "Overview of ORIGEN2 AND ORIGEN-S: Capabilities and Limitations," in *International High-Level Radioactive Waste Management Conference*, Las Vegas, 1992.

[15] S. M. Home, G. G. Thoreson, L. Theisen, D. J. Mitchell, L. T. Harding and W. Amai, "GADRAS-DRF 18.5 User's Manual," Sandia National Laboratories, Albuquerque, 2015.

[16] B. J. Smith, "Thesis on Near-Time Characterization of a Domestic Nuclear Event Using Gamma Spectroscopy," Air Force Institute of Technology, Wright Patterson Air Force Base, 2008.

[17] T. E. Miller, "Dissertation on Early Time Characterization of Fresh Nuclear Debris Using Gamma Spectroscopy," Air Force Institute of Technology, 2010.

[18] X-5 Monte Carlo Team, "MCNP - A General Monte Carlo N-Particle Transport Code, Version 5; Volume 1: Overview and Theory," Los Alamos National Laboratory, Los Alamos, 2008.

[19] G. A. Lucero, "Thesis on Prompt Gamma Spectroscopic Analysis of Nuclear Fallout to Evaluate Sensitivity to Nuclear Device Characteristics," North Carolina State University, Raliegh, 2016.

[20] J. H. Gifford, "Dissertation on Characterizing Variance in Fallout Composition Due to Uncertainty in Thermodynamic Models of Fractionation," North Carolina State University, Raliegh, 2020.

[21] Y. M. Dardenne and K. B. K. Winifred E. Parker, "Chemical Fractionation Is Not a Constant: Revisiting Bomb Vapor Chemistry," *Countering WMD Journal*, vol. Summer/Fall 2020, no. 21, p. 59/71, 2020.

[22] Japan Atomic Energy Agency, "Nuclear Data Center," Japan Atomic Energy Agency, 2022. [Online]. Available: https://wwwndc.jaea.go.jp/cgi-bin/FPYfig. [Accessed 2022].

[23] E. M. Baum, M. C. Ernesti, H. D. Knox, T. R. Miller and A. M. Watson, Nuclides and Isotopes Chart of the Nuclides Seventeenth Edition, United States of America: Bechtel Marine Propulsion Corporation, 2009.

[24] C. R. Martin, Fallout Fractionation in Silicate Soils, Washington D.C.: Defense Nuclear Agency, 1983.

[25] H. G. Hicks, "Calculation of the Concentration of any Radionuclide Deposited on the Ground by Offsite Fallout from a Nuclear Detonation," *Health Physics,* vol. 42, pp. 585-600, 1982.

[26] E. C. Freiling, "Fractionation III: Estimation of Degree of Fractionation and Radionuclide Partition for Nuclear Debris," U.S. Naval Radiological Defense Laboratory, San Francisco, 1963.

[27] C. J. Seery, Fallout Model Analysis, Long Island City: Ford Instrument Division, 1968.

[28] J. H. Norman, "Henry's Law Constants for Dissolution of Fission Products in a Silicate Fallout Particle Matrix," General Atomic Division of General Dynamics, San Francisco, 1966.

[29] P. Winchell, "The Compensation Law for Diffusion in Silicates," *High Temperature Science,* vol. 1, pp. 200-215, 1969.

[30] R. C. Smith, Uncertainty Quantification: Theory, Implementation, and Applications, Philidelphia: Society for Industrial and Applied Mathematics, 2013.

[31] G. Bonaccorso, Machine Learning Algorithms, Mumbai: Packt, 2017.

[32] E. Alpaydin, Machine Learning (Revised and Updated Edition), Cambridge: The MIT Press, 2021.

[33] J. Bell, Machine Learning: Hands-On for Developers and Technical Professionals, Indianapolis: Wiley, 2015.

[34] B. Ripley, "Package 'tree': R-Project," CRAN, 29 May 2022. [Online]. Available: https://cran.r-project.org/web/packages/tree/tree.pdf. [Accessed 2022].

[35] K. Dwyer and R. Hale, "Decision Tree Instability and Active Learning," in *Machine Learning: European Conference on Machine Learning*, Warsaw, 2007.

[36] S. Theodoridis, Machine Learning 2nd Ed.: A Bayesian and Optimization Perspective, Oxford: Academic Press, 2020.

[37] L. Breiman, "Random Forests," *Machine Learning,* vol. 45, pp. 5-32, 2001.

[38] B. Greenwell, "Package 'gbm': Version 2.1.8.1," CRAN, 2022.

[39] J. H. Friedman, "Greedy Function Approximation: A Gradient Boosting Machine," *The Annals of Statistics,* vol. 29, no. 5, pp. 1189-1232, 2001.

[40] R. Caruana and A. Niculescu-Mizil, "An Empirical Comparison of Supervised Learning Algorithms," in *Proceedings of the 23rd International Conference on Machine Learning (pp 161-168)*, Pittsburgh, 2006.

[41] R Core Team, "R: A Language and Environment for Statistical Computing," R Foundation for Statistical Computing, Vienna, Austria, [Online]. Available: www.R-project.org. [Accessed 2022].

[42] RStudio Team, "Rstudio: Integrated Development Environment for R," Rstudio, PBC, Boston, MA, 2022. [Online]. Available: www.rstudio.com. [Accessed 2022].

[43] ORTEC, "Detective-Ex/Dx-100T Portable Neutron and Gamma Nuclide Identiier: User's Manual," Advanced Measurement Technology, Inc., U.S.A., 2014.

[44] NuDat (Nuclear Structure and Decay Data), "National Nuclear Data Center," Brookhaven National Laboratory, [Online]. Available: nndc.bnl.gov/nudat3. [Accessed 13 July 2022].

[45] M. R. Smith, "Dissertation: Decomposition of Gamma Spectroscopic Measurements of Pulse-Irradiated Nuclear Materials Exhibiting Collinear Spectral Components and Nonlinear Coincidence Summing Effects," North Carolina State University, Raleigh, 2020.

[46] J. K. Shultis and R. E. Faw, Fundamentals of Nuclear Science and Engineering Third Edition, Boca Raton: CRC Press, 2017.

[47] S. Glasstone and P. J. Dolan, The Effects of Nuclear Weapons, Washington D.C.: United States Department of Defense and the United States Department of Energy, 1977, p. 6.

[48] J. P. Auxier, J. D. A. II and H. L. Hall, "Review of Current Nuclear Fallout Codes," *Journal of Environmental Radioactivity*, vol. 171, pp. 246-252, 2017.

[49] S. Singh, "Understanding the Bias-Variance Tradeoff; Image by Bill Howe, University of Washington," Toward Data Science, 21 May 2018. [Online]. Available: https://towardsdatascience.com/understanding-the-bias-variance-tradeoff-165e6942b229. [Accessed 26 September 2022].

[50] A. Jeffares, "What Is a Decision Tree," Wordpress, [Online]. Available: https://alanjeffares.wordpress.com/tutorials/decision-tree/. [Accessed 15 October 2022].